SANDIA REPORT

Microfabrication with Femtosecond Laser Processing - (A) Laser Ablation of Ferrous Alloys, (B) Direct-Write Embedded Optical Waveguides and Integrated Optics in Bulk Glass

Pin Yang, George R. Burns, Jeremy A. Palmer, Marc F. Harris, Karen L. McDaniel, Junpeng Guo, G. Allen Vawter, David R. Tallant, Michelle L. Griffith, and Ting Shan Luk

![Sandia National Laboratories logo] Sandia National Laboratories

Microfabrication with Femtosecond Laser Processing – (A) Laser Ablation of Ferrous Alloys, (B) Direct-Write Embedded Optical Waveguides and Integrated Optics in Bulk Glasses

Pin Yang and George R. Burns
Ceramics and Glass Processing Department

Jeremy A. Palmer and Marc F. Harris
Manufacturing, Engineering, and Process Development Department

Karen L. McDaniel
Modeling and Simmulation
l
Junpeng Guo and G. Allen Vawter
RF Microsystems Technologies

David. R. Tallant
Material Characterization

Michelle L. Griffith
Integrated Surety Mechanisms 2

Ting Shan Luk
DE Laser Applications

P.O. Box 5800
Sandia National Laboratories
Albuquerque, NM 87185-0959

Abstract

At Sandia National Laboratories, miniaturization dominates future hardware designs, and technologies that address the manufacture of micro-scale to nano-scale features are in demand. Currently, Sandia is developing technologies such as photolithography/etching (e.g. silicon MEMS), LIGA, micro-electro-discharge machining (micro-EDM), and focused ion beam (FIB) machining to fulfill some of the component design requirements. Some processes are more encompassing than others, but each process has its niche, where all performance characteristics cannot be met by one technology. For example, micro-EDM creates highly accurate micro-scale features but the choice of materials is limited to conductive materials. With silicon-based MEMS technology, highly accurate nano-scale integrated devices are fabricated but the mechanical performance may not meet the requirements. Femtosecond laser processing has the potential to fulfill a broad range of design demands, both in terms of feature resolution and material choices, thereby improving fabrication of micro-components. One of the unique features of femtosecond lasers is the ability to ablate nearly all materials with little heat transfer, and therefore melting or damage, to the surrounding material, resulting in highly accurate micro-scale features. Another unique aspect to femtosecond radiation is the ability to create localized structural changes thought nonlinear absorption processes. By scanning the focal point within transparent material, we can create three-dimensional waveguides for biological sensors and optical components.

In this report, we utilized the special characteristics of femtosecond laser processing for microfabrication. Special emphasis was placed on the laser-material interactions to gain a science-based understanding of the process and to determine the process parameter space for laser processing of metals and glasses. Two areas were investigated, including laser ablation of ferrous alloys and direct-write optical waveguides and integrated optics in bulk glass. The effects of laser and environmental parameters on such aspects as removal rate, feature size, feature definition, and ablation angle during the ablation process of metals were studied. In addition, the manufacturing requirements for component fabrication including precision and reproducibility were investigated. The effect of laser processing conditions on the optical properties of direct-

written waveguides and an unusual laser-induced birefringence in an optically isotropic glass are reported. Several integrated optical devices, including a Y coupler, directional coupler, and Mach-Zehnder interferometer, were made to demonstrate the simplicity and flexibility of this technique in comparison to the conventional waveguide fabrication processes.

Acknowledgement

Intentionally Left Blank

Table of Contents

List of Figures

A. FEMTOSECOND LASER ABLATION OF FERROUS ALLOYS

B. MICROFABRICATION OF OPTICAL WAVEGUIDES AND INTEGRATED OPTICS IN BULK GLASS

Appendix

List of Tables

A. FEMTOSECOND LASER ABLATION OF FERROUS ALLOYS

B. MICROFABRICATION OF OPTICAL WAVEGUIDES AND INTEGRATED OPTICS IN BULK GLASS

A. FEMTOSECOND LASER ABLATION OF FERROUS ALLOYS

By -Jeremy A. Palmer, Michelle L. Griffith, Marc F. Harris, and Karen L. McDaniel

An experimental study established parameters for accurate and repeatable femtosecond laser micromachining of ferrous alloys including AISI Type 304 stainless steel, and kovar. The central objectives are to (1) understand the ablation process of steels and to determine the correct path sequencing to drive the process and, (2) observe how changes in the incident angle of the laser beam relative to the substrate affects the accuracy and precision of percussion-drilled features. Ablation trials with varying substrate angle were conducted in vacuum and ambient atmospheric conditions. Qualitative trials were conducted to confirm the benefits of rotating polarization on feature accuracy. The last section illustrates an accelerometer product created in kovar using the femtosecond laser micromachining processes described here.

A.1 FEMTOSECOND LASER MACHINING OF STEEL

Stainless steel 304L foils were used for this work. Typically, 200 um-thick foils were used. The foils were mounted in a window frame fixture where features ablated through thickness easily fall out of the foil for analysis. Full power (975 mW) was used for most studies. Since this work involves the utilization of traditional rapid prototyping (RP) techniques, effects of travel velocity, layer decrement, and geometric features were studied. Internally-developed software was used to define the path sequence for part fabrication. Simple machine language (M and G codes) was used for initial parameter studies. Ablated features were analyzed by optical and scanning electron microscopy. Width and depth of features were measured by interferometry techniques.

A.1.1 Velocity/Feed Rate Studies

For complex part fabrication, parts must be processed in a layered manufacturing approach. A three-dimensional part is partitioned into two-dimensional cross sections and raster paths that further define each layer. In order to correctly choose the layer thickness and raster width (known as hatch) we need to understand the effect of velocity on feature width and depth. Single lines, 10 mm long, were drawn at various velocities

and their width and depth measured using interferometry. Table A1.1 shows the velocity, width, and depth for the lines drawn. Fig. A1.1 shows the morphology of the lines ablated.

Table A1.1. Effect of travel velocity on resulting width and depth of ablated line.

Velocity (mm/s)	Line Width (µm)	Line Depth (µm)
0.42	46	0
0.85	18/49	25
1.69	29/54	19
3.39	44/58	4.5

(a)   (b)   (c)   (d)
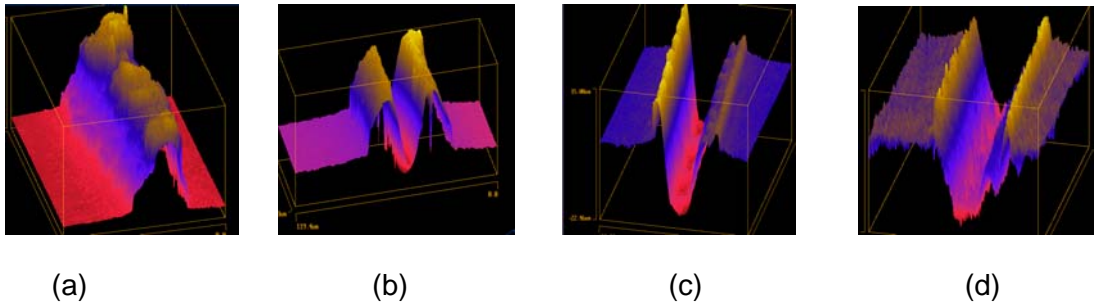
Fig. A1.1 Interferometric data showing cross-sectional morphology of lines fabricated with varying velocities: (a) 0.42 mm/s, (b) 0.85 mm/s, (c) 1.69 mm/s, and (d) 3.39 mm/s, axis scales differ for each velocity.

Depth was measured from the foil surface to an average depth within the channel. For the three fastest velocities, the first value in the line width column is the interior width, whereas the second is an indication of how much material was redeposited around the channel. As the velocity increases, this difference becomes negligible. As expected, increasing velocity results in decreasing depth with less redeposited species.

At the slowest velocity (0.42 mm/s), where one would expect the greatest depth, it appears that there is no ablation. Ablation depths are inconsistent at this velocity. Typically depth measurements are 40-50 microns for thick foils; however, plasma generation and particle collisions can inhibit the species from escaping the channel. In the current example, the ablated species decelerated and redeposited across the channel opening. It is expected, if cross-sectional microscopy were performed, there would be a slot, approximately 45 microns deep, underneath this deposition. Even though more

material is ablated at slower velocities, which could decrease fabrication time, the unreliability of clean channel formation is unfavorable for repeatable manufacturing.

A1.2 Comparison Of Parameter Sets For Component Fabrication

By utilizing a layered manufacturing approach, a three-dimensional shape is represented by two-dimensional cross-sections where each cross-section is represented by a raster pattern. There are two choices for volumetric material removal: 1) fast travel velocity and smaller layer decrement or 2) slow travel velocity and larger layer decrement. Processing speed is of great importance in the manufacturing environment, but so is final part resolution and cleanliness. Fig. A1.2 shows a micrograph of a 200-micron thick
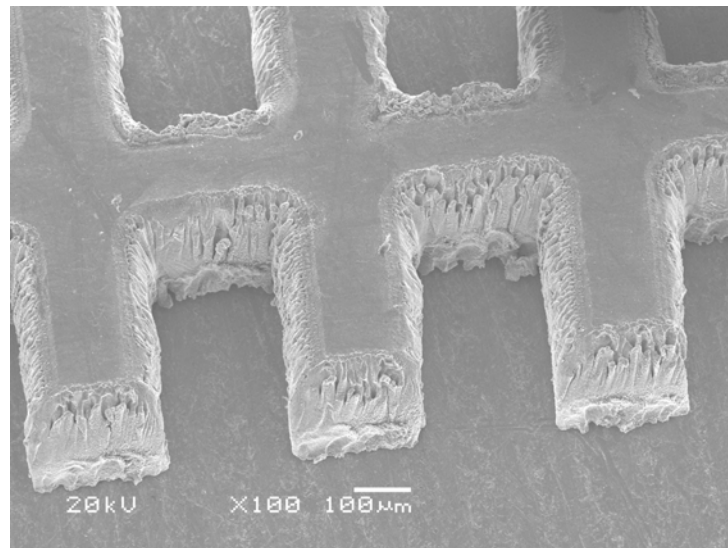
Fig. A1.2 Comb geometry fabricated at 0.42 mm/s with 25 micron layer decrements. Comb arms are 200 microns wide with 250 micron spacings.   For a 200 micron thick foil, it took 12 passes to ablate through thickness.

comb geometry fabricated at 0.42 mm/s at 25-micron layer decrements. The comb geometry is reasonably accurate dimensionally, but as the figure shows, there is a large amount of recast material along the sidewalls. Furthermore, it took twelve passes to ablate through the thickness or a discrepancy of 100 microns. This supports the concept that during fabrication some of the ablation energy is utilized to remove old material that has recast within the channel. In contrast, as Fig. A1.3 shows, a ratchet gear was

fabricated at 1.69 mm/s and 5-micron layer decrements. The gear is both dimensionally accurate and has little recast material. The gear was cut through a 100-micron thick foil in 18 passes, or 90 microns, resulting in a more efficient process where energy is directly utilized to cut features. Although the gear was cut from a 100-micron foil, it is apparent that the small layer decrement is better for part fabrication. For this parameter set, the particles can volatize away from the channel without heavy plasma shielding or increased particle-particle collisions.
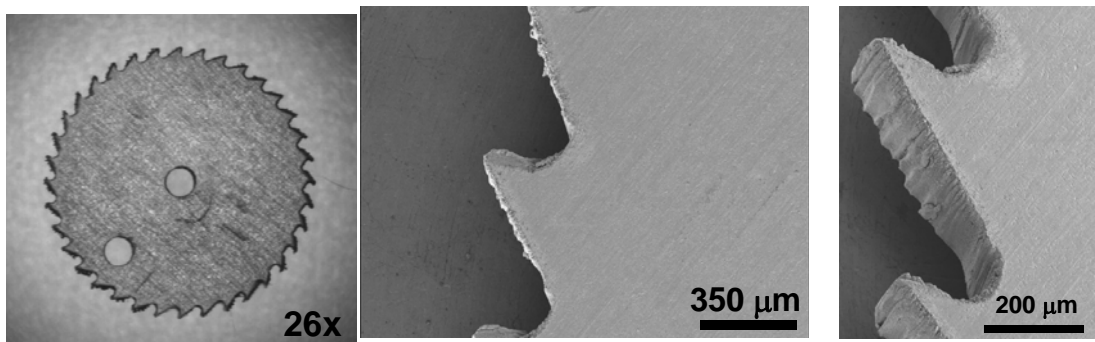
Fig. A1.3 Ratchet gear gabricated in 100 micron thick foil using the following parameters: 1.69 mm/s, 5 micron layer decrement, 18 passes to ablate through thickness.

A.2 EFFECTS OF VARYING SUBSTRATE ANGLE ON FEATURE QUALITY

Previous groups have observed optical and thermal mechanisms that induce dimensional error in short-pulse percussion drilling of metallic substrates.[1,2,3,4] Dausinger asserts that although femtosecond pulse ablations are theoretically non-thermal, secondary heat transfer effects, such as expulsion of molten material, can alter features.[1] Luft, Franz, Emsermann, and Kaspar note that these thermal effects limit precision in short pulse drilling of metals at high fluence[2]. The position of the focal point above the substrate impacts the width of laser-machined traces in metals, according to Kamlage, Chichkov, Ostendorf, and Tonshoff.[3] Nolte *et al*. demonstrate how the polarization state of the beam leads to distortion of the exit region of holes.[4] The magnitude of dimensional error is often material specific.[1,2,3,4] Comparatively few have investigated dimensional error in configurations where the substrate is oriented at an oblique angle relative to the beam. Ostendorf, Kulik, and Stute performed ablations on inclined substrates in a study of undercut features[5]. They discovered that the ablation rate on one

surface of the feature was different than that of the opposite face.[5]   This research was motivated by the question of whether the apparent non-uniform ablation is useful for improving accuracy and precision through controlled changes in the slope of the substrate. Klimentov *et al.* explored the role of the ambient atmosphere in femtosecond and picosecond laser micromachining of metals.[6]   They cite consistently higher ablation rates in a low vacuum, accompanied by a reduction in plasma and non-linear optical phenomena (so-called conical emission) at the focal point.[6]   These findings are confirmed by Pruess, Demchuk, and Stuke, who document higher vacuum ablation rates for nickel and indium substrates.[7]   Moreover, they note a reduction in recast material in a vacuum environment.[7]   Previous Sandia research achieved greater dimensional accuracy when stainless steel parts were laser micromachined at relatively high feed rates (greater than 1.5 mm/s) and lower material removal per pass.[8]   It follows that micromachining in a vacuum environment may facilitate higher feed rates (due to the greater ablation rate), less recast, and therefore greater accuracy and precision. In conjunction with vacuum, some ablation trials in this program were conducted with a localized flow of nitrogen. The conjecture is secondary process gas may boost accuracy and precision by accelerating removal of recast material from the ablation site.

The unique contribution of this work is that quantifiable standards for accuracy and precision of laser micromachined structures in angled substrates are defined and measured. Standards such as these are useful in deploying the femtosecond laser system in a production environment.   There is significant literature containing dimensional measurements of ablated features. However, there is little prior work that utilizes these measurements in insightful calculations of accuracy and precision. The next segment describes the experimental apparatus, and the scanning electron microscopy (SEM) system used to measure dimensional data. Metrics for accuracy and precision are subsequently derived.

A2.1 Methodology
        Fig. A2.1 is a schematic of the Sandia femtosecond laser process chamber. Laser energy of 1mJ at a maximum of 950 mW is provided by a Spectra Physics Hurricane™ Ti:sapphire laser. The nominal pulse width is 120 fs, with a frequency of 1 kHz. The

wavelength is 800 nm. A 20X refractive objective (numeric aperture 0.4), or a 15X Schwarzschild reflective objective (NA 0.28) focuses the beam onto an angle ablation fixture (not shown in Fig. A2.1) mounted to an Aerotech *x-y* positioning system. The minimum spot size is approximately 40 um at 975 mW .[8]

The objective is part of the *z*-axis stage assembly that provides vertical adjustment of the focal point. Secondary process gas is passed through a chamber port, and delivered to the ablation site through a 1-mm nozzle (not shown). Fig. A2.2 (a) depicts
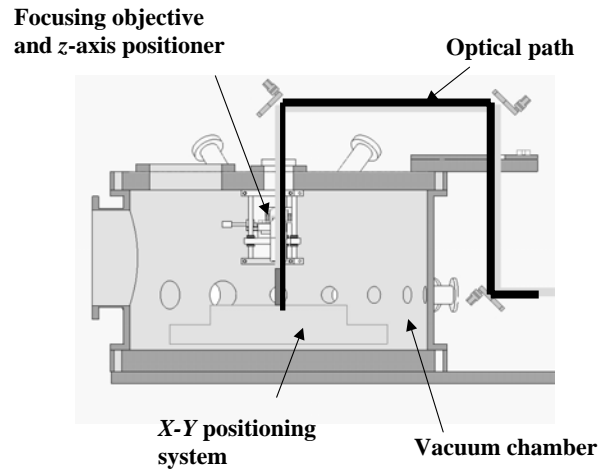
Fig. A2.1 Femtosecond laser system schematic.
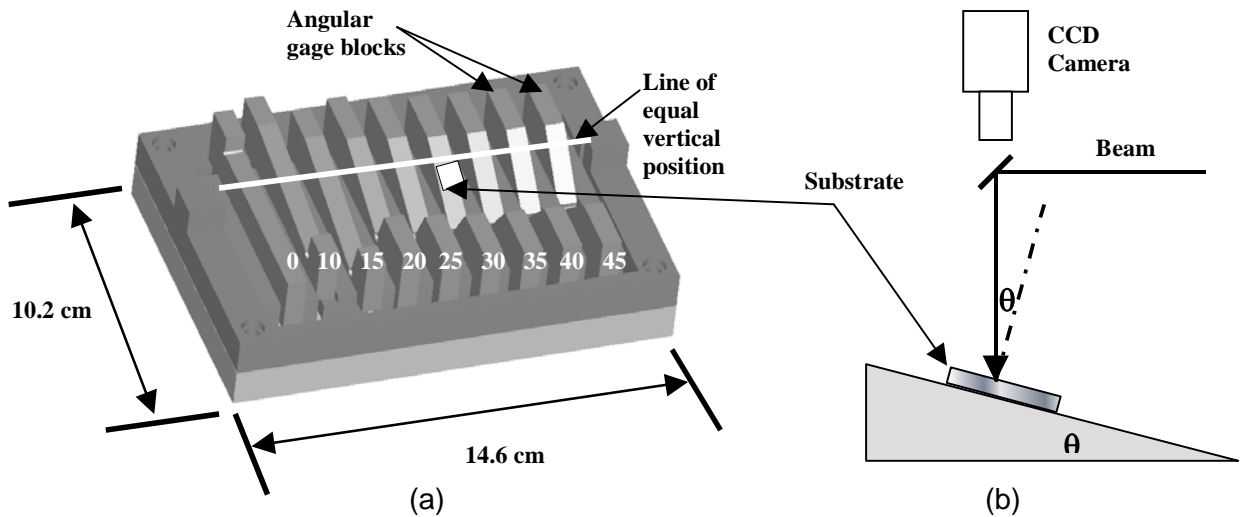
Fig. A2.2 Angular fixture: (a) isometric view with attached substrate, (b) schematic showing beam path.

the angular ablation fixture with a substrate attached. The fixture is an assembly of sloped gage blocks ranging from 0 to 45 degrees. Each block is set in the fixture such that, following alignment, a series of substrates with increasing inclination (θ) can be processed without adjusting the vertical position of the focal point. A thin layer of mineral oil or vacuum grease adheres substrates to the sloped fixture surfaces. At the start of each ablation trial, three to five substrates are arranged at increasing slopes along the line of equal vertical position (see Fig. A2.2(a)). The beam is focused on the surface of the substrates with the aid of a CCD camera (see Fig. A2.2 (b)). Hole and line features created by the laser are subsequently prepared for imaging and dimensional measurement by an SEM (FEI model XL-40 ESEM) system. SEM measurements are accurate within ± 5%.

Initial ablation trials were intended for measuring the accuracy of ablated features in sloped substrates. A secondary goal was to use Taguchi statistical processing methods to identify process parameters associated with high accuracy percussion drilling of stainless steel[9]. AISI 304 stainless steel substrates (9 mm x 20 mm), approximately 200 um thick, were loaded in the angular ablation fixture at slopes of 15, 30, and 45 degrees. Holes were percussion drilled through the substrates using the 20X refractive objective in ambient atmospheric conditions with varying fluence and exposure time. Exposure time was managed in separate trials by two methods, (1) pulse counting and, (2) "dwelling," where the beam was terminated by an electromechanical shutter after a programmed interval. Table A2.1 lists the Taguchi experimental matrices. Metrics for feature accuracy are listed in the following segment.

Metrics were derived to quantify the accuracy of the entrance hole geometry, slope of the midsection, and linearity of the midsection. Inspection of Figure A.2.2(b) reveals that the projection of the beam's circular spatial profile on the inclined substrate is an ellipse. In the ideal case, the elliptical aspect ratio, i.e. the ratio of the major diameter (*b*) and minor diameter (*a*), is given by the following:

$$\beta = \frac{b}{a} = \frac{1}{\cos\theta} \, . \tag{1}$$

Assuming there is no slope in the plane normal to the page, the minor diameter remains constant, and is determined from SEM measurement of the feature diameter when the substrate is orthogonal to the beam. The major diameter is measured in sloped substrates by the same method. It follows that the accuracy of the entrance hole geometry is the percent difference

Table A2.1 Experimental matrices for ablation trials with stainless steel.

Trial	Fluence (J/cm^2) (Power (mW))	Substrate Angle, θ, (deg)	Number of Pulses
P1	24 (300)	15	50
P2	24 (300)	30	500
P3	24 (300)	45	1000
P4	48 (600)	15	500
P5	48 (600)	30	1000
P6	48 (600)	45	50
P7	72 (900)	15	1000
P8	72 (900)	30	50
P9	72 (900)	45	500
Trial	Fluence (J/cm^2) (Power (mW))	Substrate Angle, θ, (deg)	Dwell Time (seconds)
D1	24 (300)	15	1
D2	24 (300)	30	10
D3	24 (300)	45	100
D4	48 (600)	15	10
D5	48 (600)	30	100
D6	48 (600)	45	1
D7	72 (900)	15	100
D8	72 (900)	30	1
D9	72 (900)	45	10

between the actual and ideal elliptical aspect ratio (see Eq. 1).

Accuracy of the slope of the midsection is the percent difference of the substrate inclination (θ), and SEM measurements of the slope of the midsection of the feature (θ_m). The slope measurement is taken from the wall that indicates the greatest linearity (see Fig. A2.3).

Accuracy in terms of linearity of the feature walls is calculated as follows. The Cartesian (x-y) coordinates of 10 to 20 points along the midsection of each wall are

plotted as shown in Fig. A2.3. An arbitrary point O close to the bottom of one of the walls is selected as the origin. Correlation coefficients (R^2) are calculated from linear curve fits of each set of coordinates. Accuracy is the difference of the correlation coefficient from unity (1). In practice, only the smallest difference is recorded.
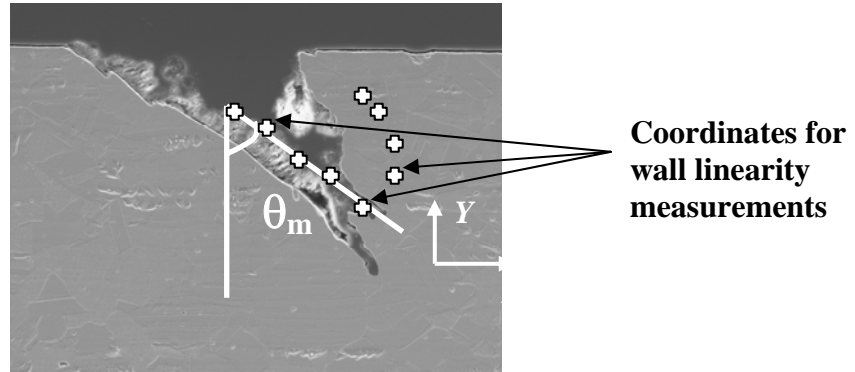
Fig. A2.3 SEM micrograph of a feature in a Kovar substrate showing locations for wall slope and linearity measurements.

A global estimate of feature accuracy is calculated from the square root of the sum of the squares of the individual metrics described above, and expressed in decibels. The global accuracy estimate was input to the ANOVA algorithm that indicated the process parameters (see Table A2.1) associated with high accuracy features.[9]

The second half of the research program considers the repeatability (precision) of features on inclined substrates. Five sets of 15 blind lines (trenches), 0.5 mm long, were percussion drilled in kovar under the conditions described below. The substrate was moved under the beam at a rate of 40 micrometers per second. Substrates were approximately 0.6 cm square, and 500 um thick. The five sets correspond to slopes of 15, 20, 25, 35, and 45 degrees as illustrated in Fig. A2.2. Following ablation, samples were prepared for SEM analysis.

Kovar trials were conducted in an ambient atmosphere, vacuum, and vacuum with constant nitrogen flow. Vacuum pressure ranged from 1 to 5 Torr. Nitrogen flow rates were limited such that the vacuum pressure did not increase beyond 5 Torr. Initial trials were conducted with the 15X Schwarzschild reflective objective, while follow-up trials in vacuum conditions were run with the 20X refractive objective (see below). Laser fluence

at the focal point H_f is expressed as the following:

$$H_f = \frac{\Phi}{\pi f \left(\dfrac{d}{2}\right)^2} \qquad \text{(J/cm}^2\text{)}\qquad\qquad (2)$$

where Φ is the laser power in watts, f is the pulse frequency in hertz, and d is the diameter of the focal spot.[13] Laser fluence in the kovar investigation was held constant. Fluence magnitude was guided by the work of Dausinger and Bonse, who recommend setting fluence slightly above the ablation threshold to reduce recast[1, 12]. Prior Sandia research reported that the threshold fluence for kovar ablated in air and vacuum ranges from 0.22 to 0.45 J/cm^2.[11] Given a spot size of 40 um and a frequency of 1 kHz, the threshold fluence corresponds to a power range of 2.8 to 5.7 mW. Based on these results, a fluence of 8 J/cm^2 (100 mW) was selected. This value is near the threshold, yet it was large enough to remove noticeable amounts of material in a single pass in ambient conditions.

SEM measurements of entrance width, maximum depth, and wall angle were recorded. It was apparent in preliminary observations that the midsection profiles of features ablated in kovar were highly irregular. Consequently, wall angles were considered near the entrance. The primary measure of precision or repeatability is given by the sample variance, the square of the standard deviation[10]. Variance data was calculated for each of the areas listed above.

A2.2 Experimental Data

This segment reports SEM measurements, and corresponding accuracy and precision data for the experimental trials described above. Table A2.2 lists data for the accuracy metrics derived in the previous section. Global accuracy estimates are reported as dimensionless and decibel quantities (see Methodology section). The smallest (most negative) values are listed in bold type.

Sample variance data for kovar ablation trials run in ambient atmosphere, vacuum, and vacuum with nitrogen flow, are plotted in Fig. A2.4, A2.5, and A2.6. Fig. A2.4 depicts entrance width variance, while Fig. A2.5 and A2.6 show maximum depth and wall angle variance, respectively.

Table A2.2 Accuracy data for percussion-drilled features in stainless steel.

Trial	Entrance Hole Elliptical Aspect Ratio Difference	Midsection Slope Difference	Wall Linearity	Global Accuracy (dimensionless, dB)
P1	0.81	0.22	0.089	0.844, -1.47
P2	0.78	0.05	0.039	0.787, -2.08
P3	0.27	0.29	0.070	0.404, -7.87
P4	0.25	0.60	0.251	0.697, -3.14
P5	0.24	0.14	0.033	0.275, **-11.21**
P6	0.17	0.72	0.021	0.738, -2.64
P7	0.11	0.07	0.019	0.132, **-17.59**
P8	1.38	0.06	0.068	1.383, 2.82
P9	0.02	0.19	0.029	0.192, **-14.33**
Trial	Entrance Hole Elliptical Aspect Ratio Difference	Midsection Slope Difference	Wall Linearity	Global Accuracy (dimensionless, dB)
D1	0.45	0.27	0.016	0.518, -5.71
D2	0.33	0.29	0.009	0.438, -7.17
D3	1.16	0.01	0.007	1.157, 1.27
D4	0.19	0.01	0.009	0.189, **-14.47**
D5	1.59	0.20	0.048	1.604, 4.10
D6	0.19	0.22	0.034	0.291, **-10.72**
D7	0.43	0.33	0.094	0.553, -5.15
D8	0.18	0.11	0.061	0.219, **-13.19**
D9	0.58	0.28	0.056	0.642, -3.85

A.2.2.1 Results

Referring to Table A2.2, parameter levels associated with high accuracy are those with the most negative averages in decibels i.e. "least is best." By invoking the ANOVA algorithm, the optimum combination of parameters can be identified[9]. This involves calculating mean global accuracy results. Consider the parameters listed in Table A2.1: laser fluence, substrate angle, number of pulses, and dwell time. Trials were conducted

for three different magnitudes, or levels, assigned to each parameter i.e. trials were run for angles of 15, 30, and 45 degrees. It follows that the mean global accuracy associated with the first level (15 degrees) of the substrate angle parameter is the average of the results for trials P1, P4, and P7, or –7.4 decibels (see Table A2.2). Mean global accuracy results are summarized in Table A2.3. The most negative values are listed in bold type, indicating the optimum parameters: laser fluence of 72 J/cm^2, 45-degree substrate angle, and 1000 pulses or the equivalent dwell time of 1 second. The relative influence of each parameter in the optimum set is out of the scope of this paper. A SEM micrograph of the feature cross section created with the optimum parameter set appears in Fig. A2.7 (a). The measured aspect ratio difference of the entrance hole ellipse is 0.194, the midsection slope difference is 0.200, and the wall linearity is 0.011. The corresponding global accuracy is 0.279, or –11.09 dB. For comparison, the feature created with the same parameters at normal incidence is shown in Fig. A2.7 (b). In this case, the midsection slope difference is 0.051, the wall linearity is approximately 0.372, and the global accuracy is 0.375, or –8.52 dB. Although the feature drilled at normal incidence is clearly more accurate in terms of midsection slope, the feature drilled at 45 degrees exhibits superior wall linearity and overall straightness.

Entrance Width Variance vs. Substrate Angle
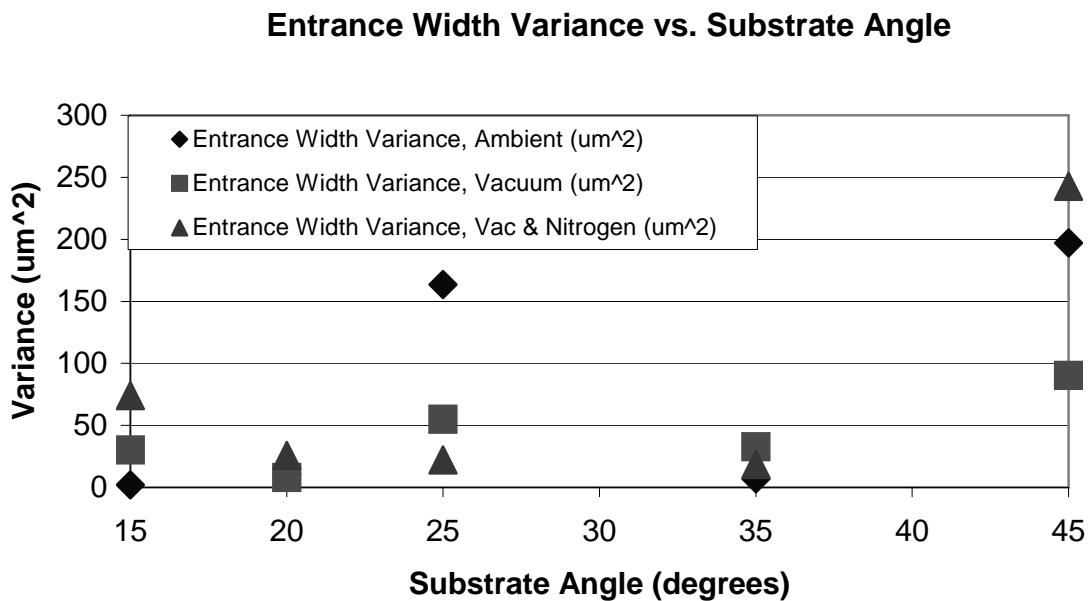
Fig. A2.4 Entrance width variance versus substrate angle for Kovar ablations in ambient and vacuum conditions.

Maximum Depth Variance vs. Substrate Angle
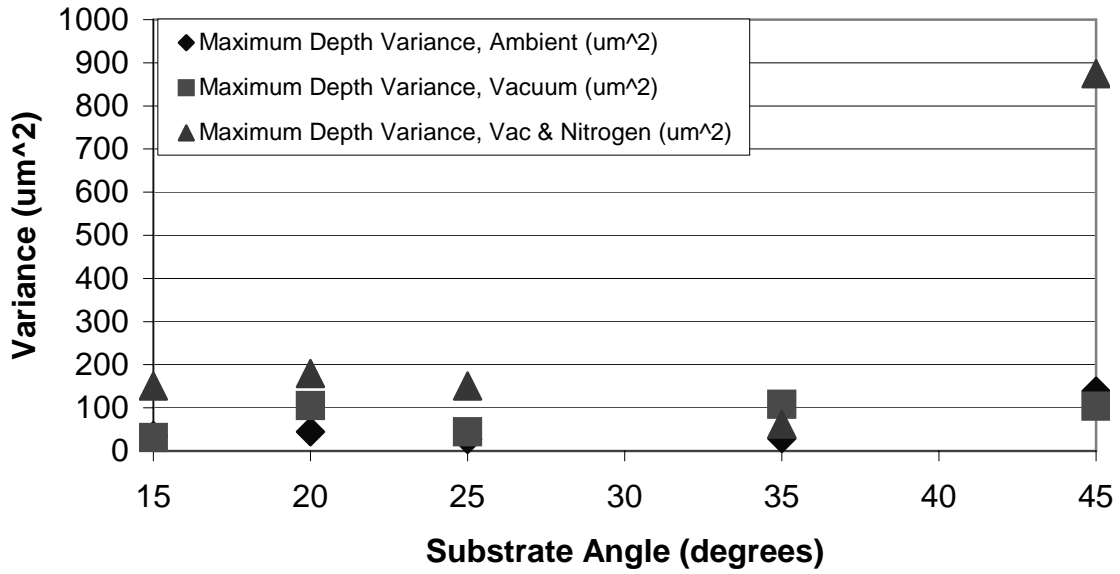
Fig. A2.5 Maximum depth variance versus substrate angle for Kovar ablations in ambient and vacuum conditions.

Wall Angle Variance vs. Substrate Angle
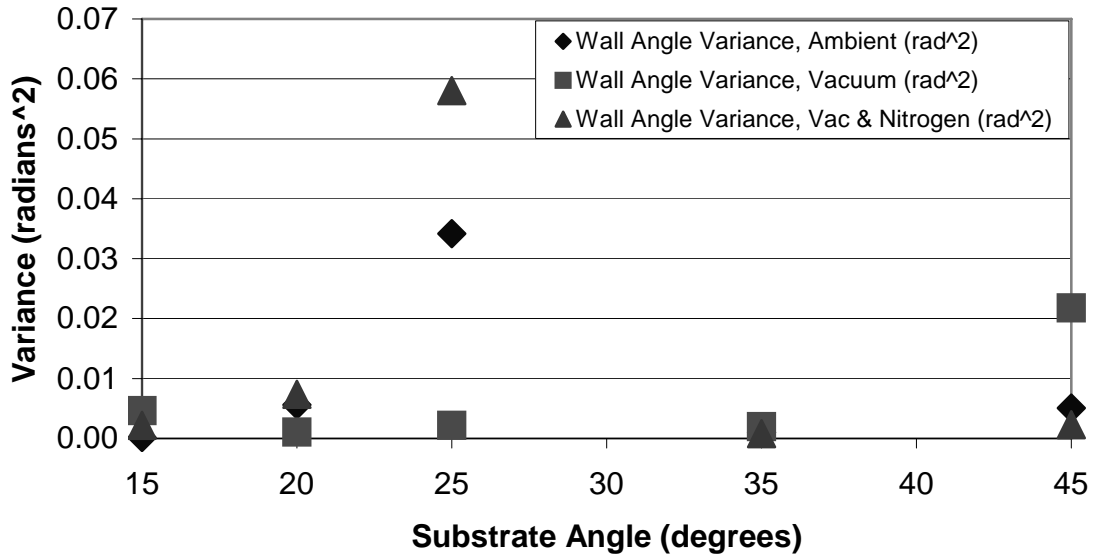
Fig. A2.6 Wall angle variance versus substrate angle for Kovar ablations in ambient and vacuum conditions.

These results indicate that percussion drilling at oblique angles with the optimized parameters may improve some elements of accuracy. However, Table A2.2 shows evidence of favorable accuracy at various substrate angles. Consequently, more work is necessary to verify these findings.

Table A2.3 Mean global accuracy results for percussion-drilled features in stainless steel.

Parameter	Magnitude, Level	Mean Global Accuracy (dB)
Fluence (J/cm^2)	24	-3.81
	48	-5.66
	72	**-9.7**
Substrate Angle, θ, (deg)	15	-7.4
	30	-3.49
	45	**-8.28**
Number of Pulses	50	-0.43
	500	-6.52
	1000	**-12.22**
Dwell Time (seconds)	1	**-9.87**
	10	-8.50
	100	0.07
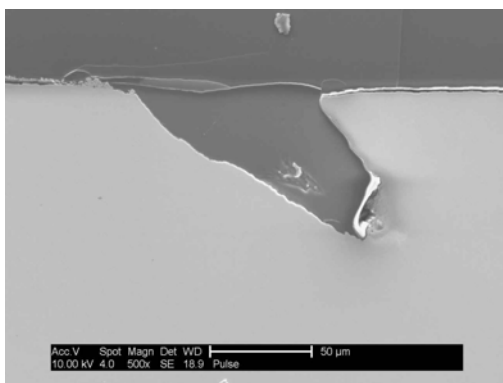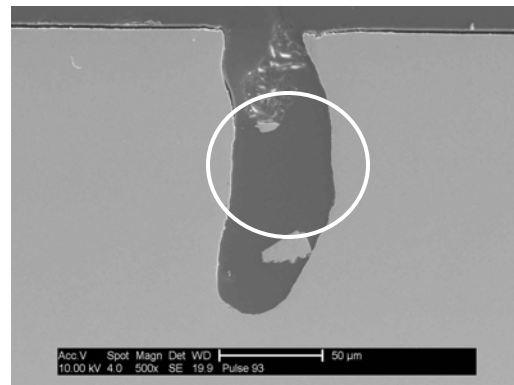
(a)   (b)

Fig. A2.7 (a) Feature ablated using optimal parameters, (b) feature with identical parameters ablated at normal incidence.

Fig. A2.8 (a) depicts a percussion-drilled feature in kovar, under ambient atmospheric conditions, and a substrate angle of 45 degrees. Fig. A2.8 (b) shows the same feature percussion drilled at normal incidence. Features created in ambient atmospheric conditions at normal incidence exhibit an entrance width variance of 0.41 um^2, a maximum depth variance of 24.38 um^2, and a wall angle variance of 0.0028

(a)   (b)
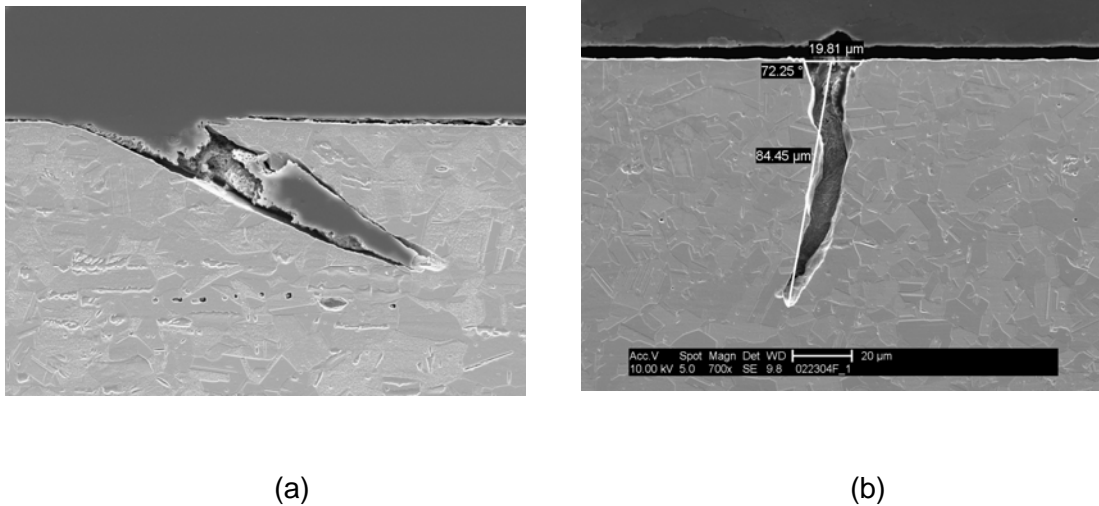
Fig. A2.8 (a) Percussion-drilled feature in Kovar (ambient atmosphere, 45-degree substrate angle), (b) similar feature, normal incidence.

radians squared. Variance was significantly greater in the case of the 45-degree substrate angle. Here, entrance width variance is 197.2 um^2, maximum depth variance is 138.9 um^2, and wall angle variance is 0.0051 radians squared. This situation is clearly depicted in Fig. A2.4 through A2.6. In each plot, features ablated at 45 degrees suffered consistently high variance in all measurement categories. Moreover, there is no apparent trend in variance with increasing substrate angle. Overall, entrance width was more precise than maximum depth. The increased variance in maximum depth is partly caused by uncertainty in the depth measurement. As Fig. A2.3 illustrates, many kovar features displayed an irregular pattern of "dendrites" in the area of the base.

Fig. A2.4 through A2.6 include variance data for percussion drilling in a vacuum, and in vacuum with local nitrogen flow. The data reveals that use of vacuum or vacuum with nitrogen flow yields little improvement in precision. However, the vacuum trials led to an important observation: kovar features that were percussion drilled in a vacuum with

the substrate velocity used in ambient conditions (40 micrometers per second) displayed significant recast and incomplete material removal. The feature in Fig. A2.9 (b) was generated in a vacuum environment with identical laser and substrate angle/velocity parameters as Fig. A2.9 (a), which was created in ambient atmosphere. The vacuum environment and the accompanying reduction in airborne plasma at the focal point apparently inhibit transport of ablation products from the substrate. In subsequent trials

(a)   (b)
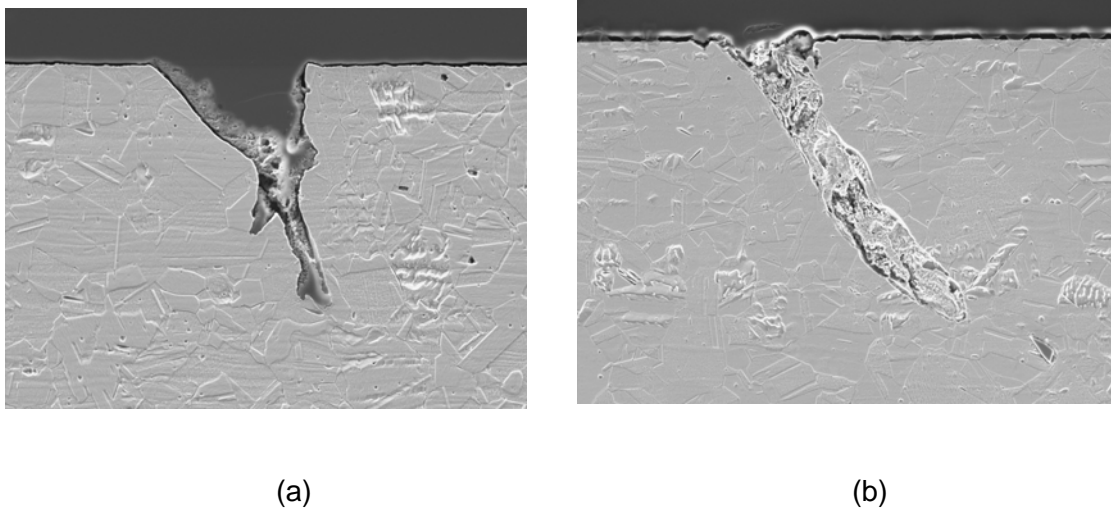
Fig. A2.9 (a) Percussion drilled feature in Kovar: ambient atmosphere, (b) similar feature drilled in vacuum (approximately 5 Torr).

with vacuum and nitrogen flow, a greater substrate velocity was used (1000 micrometers per second). Though free of recast material, the depth of the resulting features was an average of 83% smaller.

A2.2.2 Femtosecond Laser Micromachining of Kovar with Optimal Parameters

Results of the accuracy/precision study were applied in bulk micromachining mesoscale parts in kovar substrates. Two samples of a meso "windmill" are pictured in Fig. A2.10. The stainless steel sample (200 um thick) in Fig. A2.10 (a) was created in ambient atmospheric conditions with a 20X refractive objective at fluence in excess of 75 J/cm^2 (950 mW), a substrate feed rate of 420 um/s, and 25-micron z-axis steps. The comb arms are nominally 200 microns wide. Arms are separated by 250 microns. The kovar sample (150 um thick) in Fig. A2.10 (b) was generated in ambient atmosphere with a 5X refractive objective at fluence less than 30 J/cm^2 (350 mW), a substrate feed rate of

270 um/s, and 40-micron layer decrement. Columnar periodic structures on the feature walls are apparent in both cases. Fig. A2.10 (b) suggests that micromachining at lower fluence, closer to the ablation threshold, has a significant impact in reducing recast and improving wall linearity, wall parallelism and edge definition.

(a)   (b)
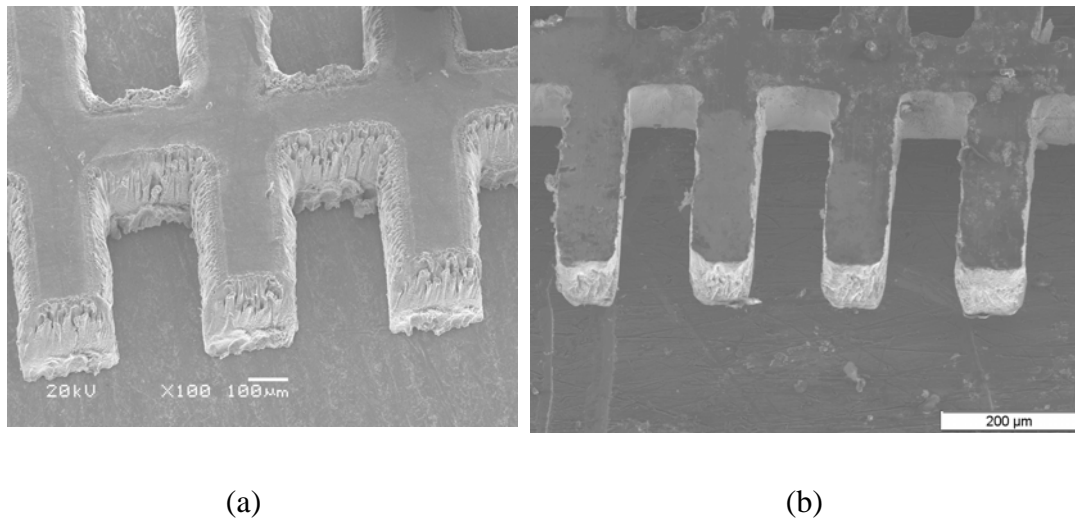
Fig. A2.10 "Windmill" bulk micromachined in ambient atmosphere: (a) 200-micron stainless steel, high fluence, (b) 150-micron Kovar, near threshold fluence.

A2.3 Conclusions and Future Work

An experimental program investigated femtosecond laser-cut features in ferrous substrates oriented at oblique angles relative to the laser beam. Quantifiable standards for accuracy and precision of these features were defined and measured. Results show improved accuracy in terms of wall linearity and overall straightness using the statistically optimized laser parameters and a 45-degree substrate angle. This shows that the femtosecond laser may be an effective tool for accurate percussion drilling of undercut structures in ferrous substrates. However, other evidence suggests that the same feature would lack precision or repeatability. Based on these results, future research in this area may explore accurate and precise deep-drilled features (with multiple passes of the beam) through programmed changes in substrate angle. Lastly, the use of vacuum and secondary process gas flow does not appear to improve precision in ferrous substrates (these findings do not address the accuracy of features generated in a vacuum environment). Furthermore, there is evidence to show that vacuum, and the diminished

focal point plasma that accompanies it, contributes to recast formation and incomplete material removal at low substrate velocity.

A2.3.1 Effects of Polarization On Feature Quality

In the nominal configuration, Ti:Sapphire femtosecond laser emissions are linearly polarized. According to Nolte et al., this condition is marked by polarization-dependent reflections from the walls of percussion-drilled holes in ferrous substrates[4]. This leads to uneven distribution of energy intensity at the focal point and ultimately non-circular geometry at the exit.[4] Polarization error can be corrected by installing optics that continuously rotates polarization, a technique known as polarization trepanning.[4] This technique was implemented in the Sandia apparatus by installing a half-wave plate polarizer driven by a DC motor at approximately 500 r.p.m. Examples of this work were incomplete at the time of publication.

A2.3.2 Product Demonstration: Accelerometer

Femtosecond laser bulk micromachining of kovar (150 um thick) was demonstrated in the Sandia sensor product shown in Fig. A2.11, below. The computer aided design (CAD) rendering of the accelerometer shown in Fig. A2.11 (a) consists of a simple proof mass suspended from a surrounding frame by four flexures. The frame is 1 inch square, while the stepped flexures are 200 microns wide at the largest segment (see Fig. A2.11(a)), and 50 microns at the smallest. Objectives of the demonstration included miniaturizing the part within practical limits and investigating the feasibility of micromachining flexures with angled walls and corresponding non-rectangular cross-section. Micromachining trials were conducted with several miniature versions of the accelerometer. In each case, the 40-micron spot size was too large to define the flexures. The example shown in Fig. A2.11 (b) was micromachined with the laser beam normal to the plane of the substrate. Most features of the sample shown in Fig. A2.11 (b) are one-fifth scale of Fig. A2.11 (a). The flexures, however, were not scaled. Alternatively, they were programmed at a width of 62 microns. Although the flexures were successfully micromachined, some did not withstand subsequent handling. Due to schedule and fixture constraints, a complete accelerometer with 45-degree flexure walls was not
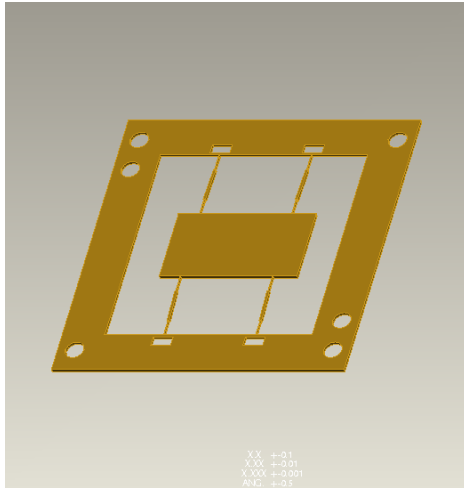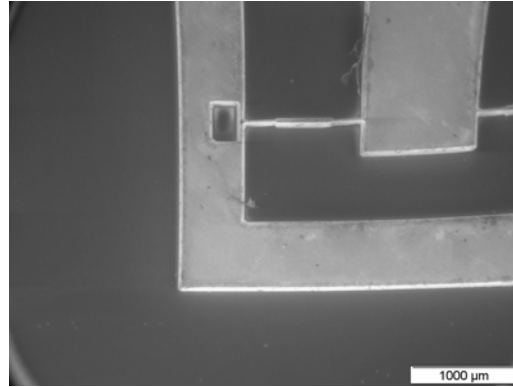
(a)   (b)

Fig. A2.11 Accelerometer bulk mircomachined from Kovar using femtosecond laser: (a) CAD rendering, (b) SEM photomicrograph of miniature version.

feasible. As an alternative, simple flexure features with 5-10 degree angled walls were micromachined and inspected. Laser fluence and substrate feed rate were similar to those used in the precision study described previously. Results are depicted in Fig. A2.12. The angled flexure walls appear sharply defined and free of recast, but lack parallelism. The reason for this is unclear.
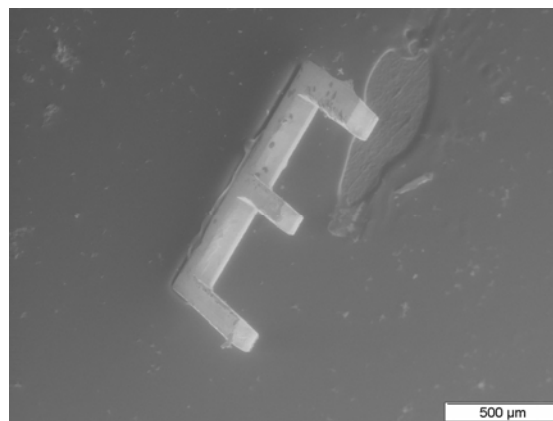
Fig. A.12 Accelerometer flexure features bulk micromachined in 150 micron Kovar at 5 – 10 degree incident angle.

A.2.3.3 Micromachining of Energetic Material Films

This LDRD program has successfully demonstrated femtosecond laser in detonation-safe micromachining of energetic material (EM) films with high accuracy and throughput. Fig. A2.13 illustrates a meso thunderbird bulk micromachined from a 7.5-micron cobalt-aluminum energetic material film. Micromachining was accomplished in vacuum (approximately 1 Torr) with a 15X Schwarzschild reflective objective, at fluence of less than 0.1 J/cm^2, a substrate feed rate of 6 mm/s. To date, femtosecond laser micromachining has been the only tool to successfully micromachine this material without detonation. Characterization work with thesesamples is ongoing.
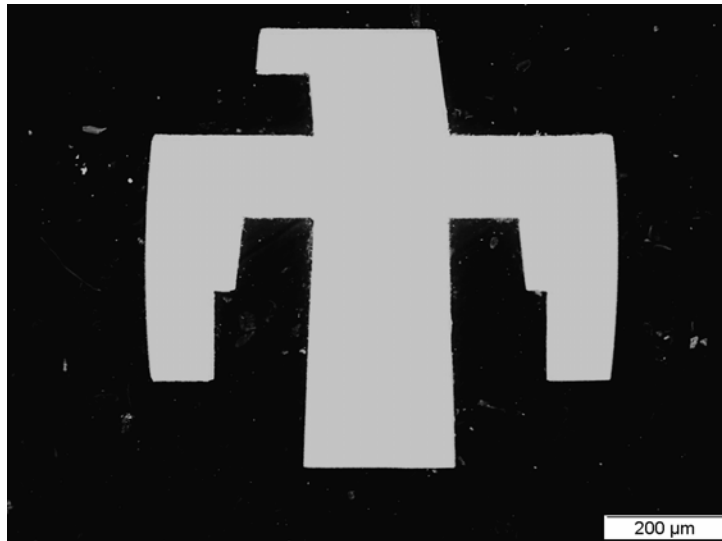
Figure A2.13 Meso thunderbird micromachined in 7.5-micron Co-Al EM film.

Figure A2.14 shows a pattern of connected porosity micromachined in a PETN trace 85-90 microns in thickness. These trials were also conducted in vacuum with the Schwarzschild objective at fluence of less than 0.1 J/cm^2. The substrate feed rate was 85 microns per second. The PETN material exhibited relatively large grains that tended to dislodge in clusters at the intersection of traces (see Fig. A2.14). This action tended to decrease dimensional accuracy at the intersections. Future work will extend femtosecond laser micromachining of energetics to include three-dimensional samples.
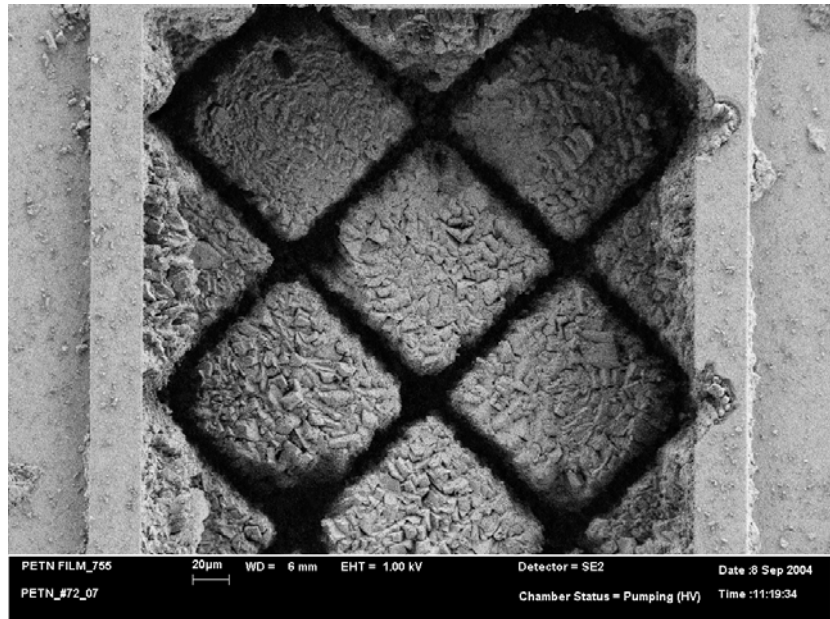
Fig. A2.14 Pattern of connected porosity micromachined in PETN energetic material film.

REFERENCES

1. F. Dausinger, "Femtosecond technology for precision manufacturing: fundamental and technical aspects," Proc. *SPIE.* **4830** (SPIE, Bellingham, WA) 471-478 (2003).

2. A. Luft, U. Franz, A. Emsermann, and J. Kaspar, "A study of thermal and mechanical effects on materials induced by pulsed laser drilling," *Journal of Applied Physics A: Materials Science and Processing*, **63** 93-101 (1996).

3. G. Kamlage, B.N. Chichkov, A. Ostendorf, and H.K. Tonshoff, "Deep drilling of metals by femtosecond laser pulses," Proc. *SPIE* **4760**, (SPIE, Bellingham, WA) 394-397 (2002).

4. S. Nolte, C. Momma, G. Kamlage, A. Ostendorf, C. Fallnich, F. von Alvensleben, and H. Welling, "Polarization effects in ultrashort-pulse laser drilling," *Appl. Phys. A*, **68** 563-567 (1999).

5. A. Ostendorf, C. Kulik, and U. Stute, "Production of innovative geometries with UV lasers," Proc. *SPIE* **4637**, (SPIE, Bellingham, WA) 280–290 (2002).

6. S. Klimentov, T. Kononenko, P. Pivovarov, S. Garnov, V. Konov, D. Breitling, and F. Dausinger, "Role of gas environment in the process of deep hole drilling by ultra-short laser pulses," Proc. *SPIE* **4830**, (SPIE, Bellingham, WA) 515-520 (2003).

7. S. Preuss, A. Demchuk, and M. Stuke, "Sub-picosecond UV laser ablation of metals," *Appl. Phys. A*, **61** 33-37 (1995).

8. M.L. Griffith, M.T. Ensz, and D.E. Reckaway, "Femtosecond laser machining of steel," Proc. *SPIE* **4977,** (SPIE, Bellingham, WA) 118-122 (2003).

9. P.J. Ross, *Taguchi Techniques for Quality Engineering: Loss Function, Orthogonal Experiments, Parameter and Tolerance design*, pp. 23-63, McGraw-Hill Book Company, New York, 1988.

10. R.S. Figliola, and D.E. Beasley, *Theory and Design for Mechanical Measurements*, pp. 117-118, John Wiley and Sons, New York, 1991.

11. D. Adams, *Micromachining with ultrashort pulse lasers,* unpublished data, 1998.

12. J. Bonse, M. Geuss, S. Baudach, H. Sturm, and W. Kautek, "The Precision of the Femtosecond-pulse Laser Ablation of TiN films on Silicon,"*Appl. Phys. A,* **69 [Suppl.]** S399-S402 (1999).

13. Rockwell Laser Industries, *Laser Safety*, pp. b4 – b7, Rockwell Laser Industries, Cincinnati, 2003.

B. MICROFABRICATION OF OPTICAL WAVEGUIDES AND INTEGRATED OPTICS IN BULK GLASS

(Pin Yang, George R. Burns, David R. Tallant, Jungpeng Guo, Ting Shan Luk, and G. Allen Vawter)

B1 INTRODUCTION

The development of an ultrahigh peak power laser pulse up to the terawatt (TW) level by a chirped pulse amplification technique[1] opens up new possibilities for micro-fabrication of three-dimensional (3D) features inside of transparent materials. These compressed laser pulses (with pulse widths less than 1 pico-second), typically are not absorbed by the transparent media in the near-infrared range (800 nm) through a single photon process due to a large band gap between the conduction band and valence band in these materials. However, when the laser beam is focused and local power density (or irradiance I) exceeds 0.5 TW per cm^2 the energy of these photon pulses can be absorbed near the focal point through a non-linear, multi-photon absorption process.[2] Since the probability of excitation of n electrons by a multi-photon absorption is proportional to the nth power of the irradiance of the light,[3] within an ultra-short time span and an immense irradiance ($I > 10^{18}$ W/m^2, 120 fs, 1 µJ/pulse) only electrons created at the laser focused point can be excited into the conduction band. In addition, the optical field accompanied with such a high irradiance level is enormous ($E \sim 10^{11}$ V/m), which triggers an additional absorption mechanism due to the generation of higher energy photons through a nonlinear self-phase modulation process. This localized absorption changes the physical and chemical properties of the transparent media and permits direct-write 3D structural modification and microstructuring by scanning the focal spot inside of the materials.

In addition to high energy laser ablation on the material surface,[4,5,6] the first application based on this physical phenomenon for fabricating embedded features in transparent bulk materials was the creation of a 3D optical data storage.[7,8,9] Submicrometer size cavities were created in the transparent materials, such as fused silica, quartz, and sapphire by the femtosecond laser pulses due to micro-explosions, generating a large index refraction contrast between glass and voids. Binary information

could later be read out with a microscope objective. This enabling feature has been explored to construct photonic lattices in transparent media such as plastics[10], composites[11], and glass.[12] In addition, a similar approach using the immense localized heating generated by the femtosecond laser pulses to selectively nucleate frequency-conversion crystals (β- BaB_2O_4) in a glass ceramic host (BaO-Al_2O_3-B_2O_3 glass) was demonstrated.[13] The first direct writing of optical waveguides in a Germanium doped silica glass by a femtosecond laser was reported in 1996.[14] Microellipsometer measurements on these photo-damaged regions showed a significant increase in index of refraction (from 0.01 up to 0.035). The formation of several laser-induced defects in glass, including Si E' or Ge E' centers, nonbridging oxygen hole centers, and peroxy radicals, were also identified. Later on, Miura et. al.[15] reported that high quality optical waveguides could be fabricated in a fluoride glass. The results of atomic force microscopy suggested that localized heating and structural rearrangement on the laser modified regions might contribute to the densification and refractive index changes. It is well known that waveguides created on the surface of a photosensitive germanosilicate glass by a short wavelength excimer laser disappear when laser-induced defects are removed at a higher temperature (> 550°).[16] In contrast, waveguides created by the femtosecond laser remain intact after the same thermal treatment. The ability to create a "permanent" index refraction change by a femtosecond laser has fueled a thrust of research and development activities to fabricate integrated optical devices.[17,18,19]

Recent advancement in this research area focused on direct-write microstrcturing in bulk glass. It was found that the femtosecond laser irradiated areas exhibit a high etching selectivity, therefore, permitting the fabrication of embedded channels or movable parts in a photosensitive glass (Foturan[TM]; Schott Glass Corporation). [20,21] In addition, the use of a continuum (white light) generation created by self-phase modulation in water to assist micromachining of 3D features from the rear surface of a silica has been demonstrated.[22,23,24,25] These new enabling microfabrication techniques open up an untapped potential to fabricate novel integrated optical systems with 3D embedded channels and advanced optical sensing capabilities. In this report, we focused our effort on direct-writing waveguides and integrated optics in amorphous silica, using a femtosecond laser. Special emphasis was placed on the effects of glass composition and

processing conditions on optical properties of these waveguides created by the femtosecond laser pulses. Preliminary results on 3D microstructuring of Foturan glass are also reported.

Embedded waveguides can be created by moving the focal spot with proper pulse energy inside of a bulk glass. These waveguides can be directly written either transversely or longitudinally to the beam direction (see Fig. B1.1). Waveguides written by a longitudinal approach[1,26] with a tight focus lens (a large numerical aperture and a short focus length) have a symmetrical cross-section. However, the depth of writing is limited by the focal length of the microscope objective. When a loose focus lens (low magnification and long focus length) is used and laser irradiance is greater than the self-focusing threshold, laser induced solid-density plasma, plasma channeling, and small filaments can be produced.[27] Figure B1.2 (a) illustrates this plasma-self channeling phenomenon duplicated in our femtosecond laser laboratory. The laser was focused near to the glass surface (as shown by a bright spot) and guided for a distance longer than the Rayleigh range in the bulk glass (as shown by the plasma generated in glass). The phenomenon has been interpreted as a counterbalance of the
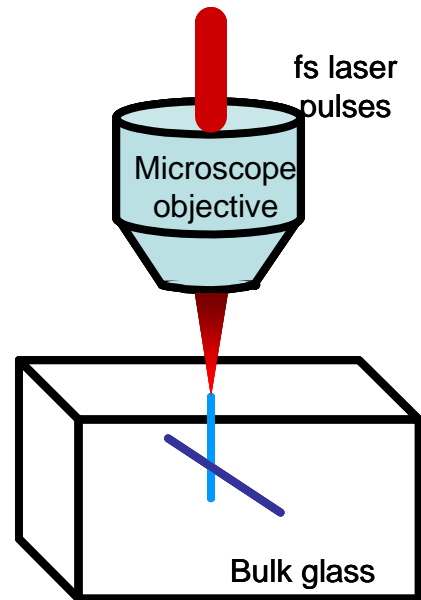
Fig. B1.1 Schematic illustration of direct-writing optical waveguides in bulk glass by femtosecond laser pulses.
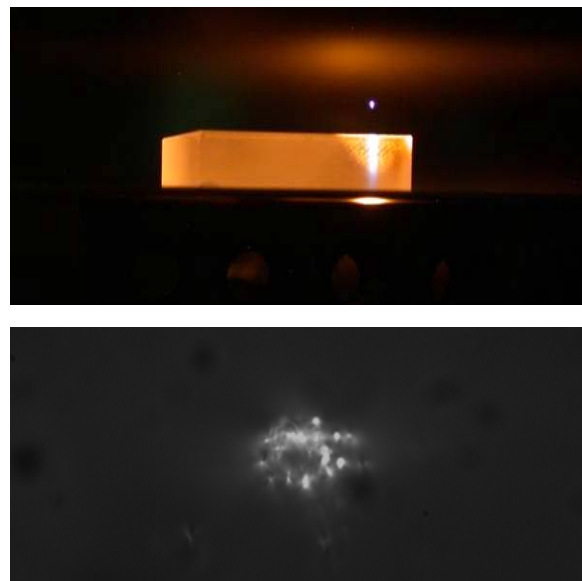
Fig. B1.2 (a) A side view of plasma self-channeling in the bulk silica glass, (b) the cross-section view of a self-channeling waveguide, showing the non-uniform structure created by the filaments (under a cross-polarized light condition).

self focusing due to the Kerr effect and the defocusing effect due to the formation of a low density plasma.[28] However, due to the formation of filaments in thelaser modified region (Fig. B1.2 (b)) the quality of the waveguide is highly non-uniform. Therefore, in the early evaluation stage, this approach was dropped out from further investigation. The transverse writing approach is convenient and has less constraint imposed by the focal length of the microscope objectives, but the intensity profile at the focal spot is elongated along the beam direction, which creates an asymmetric cross-section for the waveguides.[29] Approaches to reduce this asymmetric beam profile, either by introducing beam shaping optics[11] or a parallel slit[30], have shown great success. In this report, we used a transverse writing approach to create waveguides in amorphous silica, without introducing additional beam shaping processes. The properties of these waveguides with respect to the laser processing conditions are reported. A few prototype devices were fabricated to demonstrate the waveguide quality and the flexibility of this direct-write technology.

Two different approaches have been developed to deposit the photon energy into glass and induce localized refractive index change. The first approach uses a high-repetition-rate (MHz range), low-peak-power laser pulses which have just enough laser irradiance to cause multiphoton absorption in glass. This approach generates localized bulk heating[31] and densification, which creates an isotropic refractive index change in bulk glass (see Fig. B1.3). The second approach employs a low-repetition-rate (KHz range), high-peak-power laser pulses. This approach breaks chemical bonds, generates nonbridging oxygen hole centers,[4] modifies the silica network,[32] and creates localized refractive index change in glass. It is also found that this high-peak-power pulse approach can induce unusual birefringent properties[6,33,34] in laser-modified regions. The fundamental mechanisms for this unusual birefringence created by the intense femtosecond laser pulses in the bulk glass are not clear. In this report, experimental evidence that could contribute to the laser-induced birefringence in bulk glass will be presented and discussed.
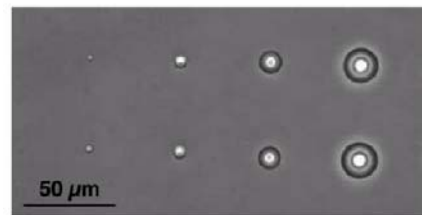
Fig. B1.3. Optical microscope image of structural produced by a high frequency oscillator (25 MHz). (C. B. Schaffer et.al.)

B2 EXPERIMENTAL PROCEDURE

The laser used in this experiment was a regeneratively-amplified Ti:Sapphire femtosecond pulsed laser (Spectra-Physics, Hurricane). The femtosecond laser pulses had a 125-femtosecond pulse-width (FWHM) and 1 kHz pulse repetition rate. The energy of the pulse could be varied by the combination of a half wave plate and a thin film polarizer. Further energy reduction was accomplished by the use of neutral density filters to avoid photo-damage to the polished glass plates. The average laser power used in this investigation was between 450 µW and 900 µW, corresponding to a pulse energy between 0.45 µJ and 0.9 µJ. The laser was focused to a 3 µm diameter spot inside the glass, using a long-working-distance microscope objective (Mitutoyo, 20X, NA = 0.40). The calculated peak intensity of the femtosecond pulse was 9.8 X 10^{20} W/m^2 for a pulse energy of 0.9µJ.

In this investigation, a thermally treated chemical vapor deposited (CVD) amorphous silica plate (Quartz International, Albuquerque, NM) was used. These glass plates, in contrast to fused quartz plates which typically have a small, yet detectable, birefringence induced by the forming process, are optically isotropic before laser writing. The glass plate (polished on both surfaces) was mounted on a motorized x-y translation stage with linearly controlled motion along the z-direction to adjust the focus of the laser inside the glass. The laser was focused approximately 600 µm below the surface of the glass plates. In addition to these linear motion controls, the sample could also be rotated in the x-y plane on a rotational stage. In the writing process for the laser-induced birefriengence study, the polarization direction of the beam was fixed, and the sample was rotated with respect to the polarization direction of the laser beam. By moving the laser focus spot perpendicular to the beam direction (20 µm/s) with an appropriate energy level (0.45 to 0.9 µJ per pulse) inside of bulk glass, optical waveguides can be created. The general quality of these waveguides was studied by near-field and far-field methods.

After laser writing, the samples were evaluated using a transmission microscope (Olympus BH-2). Samples were illuminated using a monochromatic light filtered from a halogen lamp. The filter has a center wavelength of 671 nm and a bandwidth FWHM of 10 nm. The samples were put between two crossed polarizers on the rotating stage of the

microscope. The angular rotation of the sample with respect to the polarizer was accurately measured by the stage goniometer. The transmitted light through the samples was captured by a digital camera attached to the transmission microscope viewer. Optical transmission signals were evaluated using a National Instruments PCI-1424 digital image capture card. The CCD camera is operated in the linear regime. The maximum intensity of the transmitted light for the laser-modified region was determined by scanning the image array for the maximum value in each of ten images. The values were then averaged and recorded.

Six different optical grade glasses were investigated. The composition, soft point (T_s), and glass transition temperature (T_g) of these glasses are tabulated in Table B.I. The SF2, SF4, and SF67 are high lead glass fabricated by Schott Glass (Duryea, PA). The compositions of these glasses were quantitatively determined by an electron microprobe analysis. However, the exact compositions of each commercial glass were primarily used for correlating and analyzing experimental results only; therefore, the exact values and minor additives were not tabulated in Table B.I to protect the proprietary information of manufacturers. The fused quartz, CVD quartz, and Pyrex glass all consist of a high percentage of glass former and tend to form extensive 3D networks of silica tetrahedral.

Cations, such as Si^{+4}, B^{+3} and sometimes Al^{+3} from oxygen polyhedra (triangles and tetrahedra), are called network formers. They strengthen the structure of the glass network. As a result, these glasses have a higher glass transition temperature and soft point. Alkali and alkaline cations whose major function is providing additional oxygen ions which modify the network structure are called modifiers (refer Fig. B2.1). They occupy random positions distributed through the structure and create non-oxygen bridging bonds to provide local charge neutrality. As a result, glasses having a large amount of glass
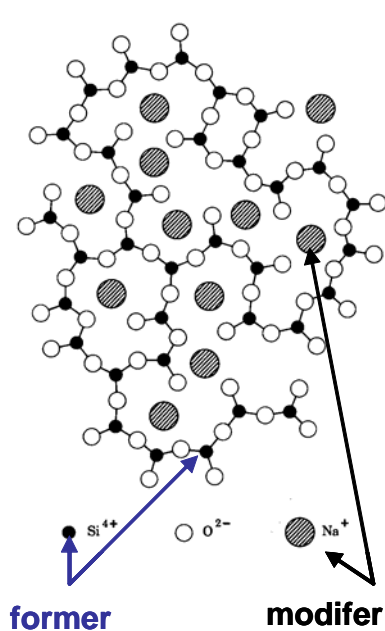
Fig. B2.1 A schematic illustration of silica network, with glass fomer and glass modifer.

modifiers tend to form a more open structure and possess a lower glass transition temperature.

Table B.I: The glass composition (in weight percent), soft point and glass transition temperatures of different glass studied in this report.

Glass	Glass Former	Glass Modifier		Other Oxides	Ts, (°C)	Tg, (°C)
	SiO_2, B_2O_3, Al_2O_3	Na_2O, K_2O	MgO, CaO,BaO, ZnO, PbO			
Fused quartz	99.97	0.00	0.03	0.00	1250	
CVD quartz	100.00	0.00	0.00	0.00	1260	
Pryex	96.37	3.57	0.06	0.00	820	560
SF2	44.79	6.46	48.74	0.01	600	441
SF4	33.82	2.03	64.12	0.03	552	420
SF57	26.43	0.61	72.96	0.01	510	414

The laser-induced local structural modification was analyzed, using the microscope accessory to the Raman spectrometer and the 458 nm laser line as an excitation source. A microscope objective focused the excitation laser into the glass and collected 180° backscattered light for dispersion and detection by the spectrometer. Collected light was dispersed by a triple monochromator and detected by a charge-coupled detector. The volume sampled using this micro-Raman technique approximates a cylinder of 1 µm diameter and 3-6 µm in depth, which is perpendicular to the laser writing direction of the modified region.

B3. RESULTS AND DISCUSSION

B3.1 Processing Condition and Structure Modification

Because of the nonlinear absorption mechanisms involved with the femtosecond laser process, photon energy can be focused deep inside of bulk glass and alter the local glass structure and create refractive index change. If the irradiance (or powder density) of the laser is below the threshold level of multi-photon absorption, glass becomes almost

transparent to the laser beam. Conversely, if the irradiance of the beam is too high, it can easily create optical damage inside of the glass.[7,35] Therefore, it is important to identify the proper processing space that can effectively change the refractive index without creating damages in the glass. It was found that the threshold of pulse energy that can create a detectable waveguide pattern by the nonlinear absorption processes is slightly above 0.2
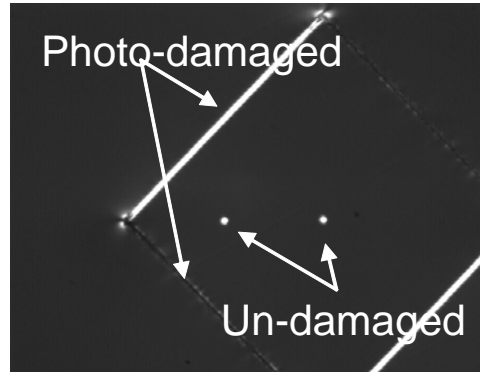
Fig. B3.1.1 Microphotograph of laser damaged and undamaged regions under a cross-polarized light condition (0.25 mm X 0.25 mm square).

µJ per pulse. Embedded waveguides without significant scattering loss can only be fabricated with pulse energy between 0.45 to 0.90 µJ.[36,37] Above this energy level, stress birefringence and sometimes microcracks can be observed, indicating photo-damage to the bulk glass. Fig. B3.1.1 shows laser-induced microcracks and stress-induced birefringence on the edges and at corners of a square test pattern under a cross-polarized light condition, when pulse energy is much greater than 1 µJ/pulse. In contrast, two spots (near the center) created by an accumulated 60,000 pulses at 0.45 µJ/pulse exhibit no detectable cracks or stress birefringence. Furthermore, experimental results indicate that the photo-damage threshold in silica is extremely sensitive to the change of laser pulse width.[38]

Difficulties were experienced when creating refractive index changes on the glass surface. Attempts using different optics and power levels to write surface waveguides were unsuccessful. It was found that a minimum optical penetration depth is required. Results show that embedded waveguides or refractive index modification can be created when the focal point is below 15 µm from the surface of an amorphous silica plate. Because the band gap of silica is large (~ 9.0 eV), the probability for multiphoton absorption directly from 800 nm wavelength photons (E = 1.55 eV) is minute since it requires at the minimum simultaneous stacking of 6 photons to cross the band gap. However, the optical field created by the femtosecond pulses is tremendous (~ 10^{11} V/m), which generates a strong nonlinear polarization and the index of refraction of the glass

becomes intensity dependent.   As a result, the phase (φ) that propagates through a optical medium with a thickness L will change according to

$$\varphi = \frac{2\pi}{\lambda} L(n_0 + n_2 I) \qquad (1)$$

, where λ is the wavelength of the incident light, n_o is the refractive index of glass in the absence of a strong optical field, and n_2 is the coefficient of an additional contribution induced by the nonlinear polarization from an immense optical field. The phase shift ($\Delta\omega$), as described by the change of phase in the optical media with respect to time, can then be expressed as

$$\Delta\omega = -\frac{d\varphi}{dt} = -\frac{2\pi}{\lambda} Ln_2 \frac{dI}{dt} \qquad (2).$$

Assuming the intensity of a femosecond laser pulse has a Gaussian profile (see B3.1.2 (a)), the phase shift in the font of the pulse increases (blue-shift; or shifting to a higher frequency), according to Eq. (2) since *dI/dt* is negative (Fig. B3.1.2 (b)). Conversely, at the back of the pulse the phase lags behind ($\Delta\omega < 0$) and generates a red-shift (shifting to a lower frequency). As a result of these phase shifts induced by a femtoseocnd laser pulse, a continuum optical spectra (white light, ranging from the UV to the near IR) can be produced in a transparent material. This physical process in changing or modulating the excitation wavelength is defined as "self-phase modulation".[39] However, a recent study suggested that the free-electron generation in condensed media by femtosecond laser pulses due to multiphoton excitation from the valence band to the conduction band induced is the primary mechanism in boarding the white light spectra (which includes both the blue- and the red- shifts). [40]   Regardless of the fundamental mechanisms, the requirement for a minimum depth in creating waveguides in silica suggests that photon energy must have been absorbed near the focal spot by two to three high energy photons created by the blue-shift of the 800 nm laser as the intense pulses propagated through the optical media.
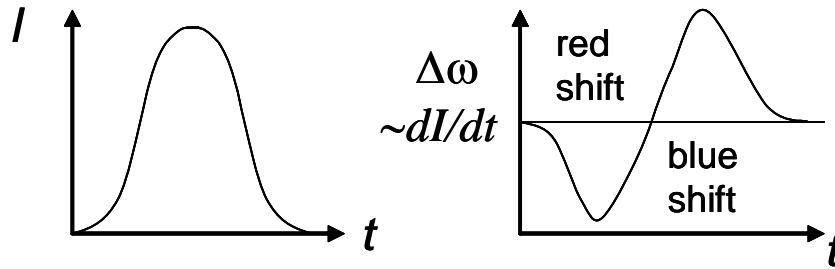
Fig.B3.1.2 A schematic illustration of a self-phase modulation process.

B3.2 Structure Modification by the Femtosecond Laser Pulses

The local glass structure modification by the femtosecond laser pulses was initially studied by optical absorption difference spectra and photoluminescence (Appendix A and B). However, results based on these preliminary studies on the laser damaged areas were not conclusive due to the difficulties in separating a large scattering of the incident beam in a standard transmission measurement during optical absorption study and a few unidentified spectra in the photoluminescence measurements. Detailed study of the structure modification was then turned over to Raman spectroscopy since the vibrational spectra of amorphous silica networks was well established. Before presenting the experimental observations, a brief introduction of the vibrational spectra (Fig. B3.2.1, see ref. 42) of amorphous silica is reviewed.

Based on a vibrational-band limits calculation, Galeener[41] assigned the dominant Raman peak to a singular matrix element rather than a peak in the density of vibrational states. The study attributed the origin of each dominant Raman line for the amorphous silica as follow,

(1) W_1 at 432 cm^{-1}: a symmetrical stretching motion as indicate by moving in B direction (see Fig. B3.2.1 (a)). Sometimes, this motion is defined as the "breathing" mode of silica rings.

(2) W_2 at 982 cm^{-1}: an asymmetrical stretching motion which an IR active mode in S direction (see Fig. B3.2.1 (a)).

(3) W_3 at 800 cm^{-1}: a rocking motion of the oxygen atom in-and-out of the base plan.

(4) W_4 at 1065 cm^{-1} and 1200 cm^{-1}: a symmetric stretching of the bridging oxygen which depends on the mass ratio between oxygen and silicon (or other network former).

Later, Galeener et. al. used an energy minimization argument[42] and identified two vibrational decoupled planar rings[43] in glass. These small planer rings show characteristic lines at 606 (D_2) and 495 cm^{-1} (D_1), representing 3-fold and 4 fold silica rings, respectively.
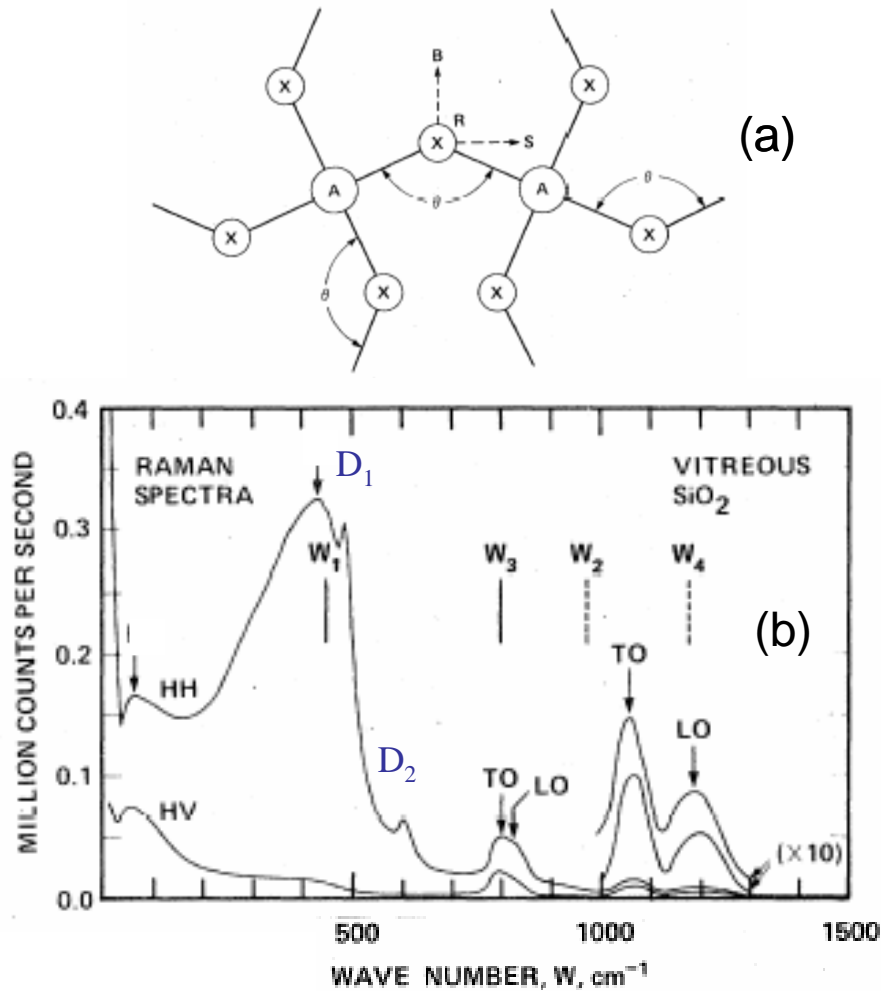
Fig. B3.2.1 (a) A schematic diagram of local oder assumed for tetrahedral AX_2 glass. (b) Raman spectra of vitreous SiO_2.

B3.2.1 Local structural Change in Laser-Damaged Regions

Figure B3.2.2 shows the micro-Raman spectrum of bulk fused quartz and normalized spectrum of a laser-damaged region (0.1 mJ). Under a cross-polarized light condition, the damaged regions exhibit stress birefringence and are occasionally associated with microcracks (refer Fig. B3.1.1). Without the normalization procedure, the intensity of the Raman bands from the laser-damaged region is consistently less than

that from the bulk glass. This reduction in intensity indicates that the modified regions have structures of lower density where some glass has been partially replaced by voids. Furthermore, the normalized Raman spectra show an increase in the 490 (D_1) and 605 cm^{-1} (D_2) peaks in the damaged region, indicating an
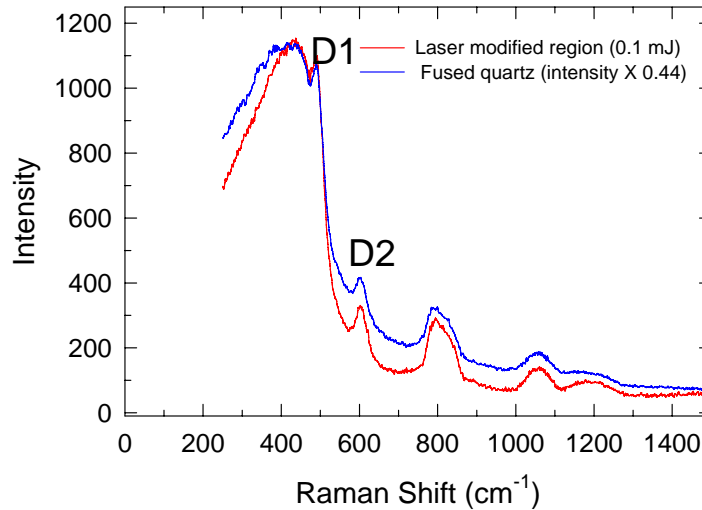
Fig. B3.2.2 Micro-Raman spectra of laser damaged region in fused quartz.

increase in the number of 4- and 3- membered ring structures[42, 44] in the silica network. Although the increased intensity in D_1 and D_2 peaks has been generally attributed to an irreversible structural change of the silica network under an extremely high pressure[44] (>30 GPa) or by a shock-wave densification[45], Tallant et. al. has demonstrated that the formation of these 4- and 3- ring structures is genuinely associated with the creation of new quasi-surfaces at small voids in the silica-rich matrices.[46] Experimental evidence, including the Raman study of a high surface area silica gel and a chemically leached borosilicate glass, has strengthened their argument. Therefore, it is believed that the increased intensity in D_1 and D_2 peaks in the laser damaged areas could be attributed to the formation of 4- and 3- silica rings due to the creation of new surfaces by the irreversible physical damages (the same argument applies to the damages induced by an ultra-high pressure condition or a shock-wave densification process). Furthermore, the creation of the quasi-surface is consistent with a lower Raman density observed at the laser damaged areas. Direct evidence based on a scanning electron microscopy study (Fig. B3.3.5) at the laser damaged regions is presented in section B3.3, where pertinent discussion with other indirect observations is documented. In addition, the Raman band

peaking between 400 and 500 cm^{-1} is significantly narrower in the spectra from laser-modified regions compared to the bulk glass. A similar behavior is also observed for the laser-modified region in Pyrex glass. The relative narrowness of the bands in the spectra indicates that the silica networks in these areas have a smaller distribution of ring sizes, with fewer large rings. This type of modification of the silica network is typically achieved by quick melting followed by fast re-solidification during the laser process. The relatively high melting points of fused quartz and Pyrex due to an extensively 3D silica tetrahedral network in the glass contributed to their fast re-solidification.
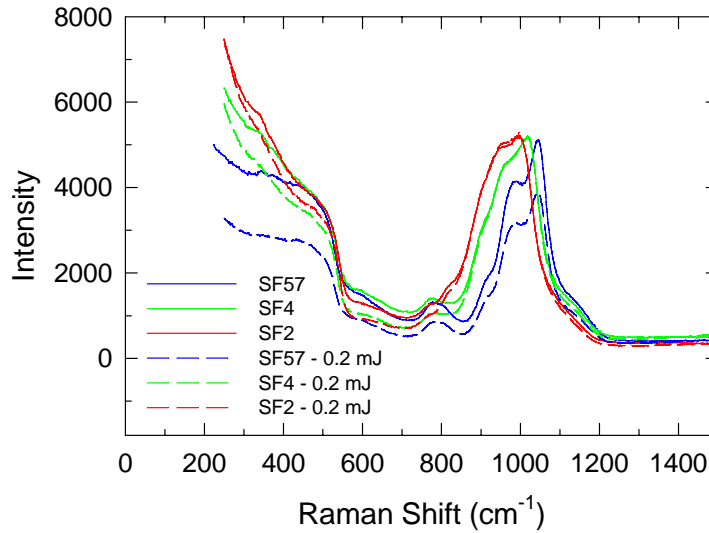
Fig. B3.2.3 Micro-Raman spectra of laser-damaged regions in lead containing glass (SF2, SF4, and SF57). The dotted and solid lines represent Raman spectra with and without laser damages, respectively.

In contrast, glasses with a higher concentration of glass modifier (Fig. B3.2.3) show less effect in the changes of the Raman bands intensity at a laser-damaged region. However, a significant change in the Raman intensity can be observed below 500 cm^{-1}, suggesting a change of the silica network in these glasses. In addition, the change of Raman intensity below 500 cm^{-1} for these glasses decreases with decreasing T_g. The smaller change in the Raman spectra can, therefore, be attributed to the lower melting point (and T_g) of these glasses, where the structural relaxation occurs at a much faster rate.

B3.2.2 Local Silica Network Structural Change in Laser-Modified Regions

Figure B3.2.4 summarizes the Raman spectra data of laser-modified regions from the Pyrex glass samples, where the laser energy is below photo-damage threshold.

Results show that the overall reduction of the intensity of Raman bands becomes significantly less in comparison to the laser-damaged regions. Similar to the photo-damaged area, the small reduction of the intensities of Raman bands can be contributed to the creation of voids in the laser-modified areas. In addition, the 445 cm^{-1} band in the spectrum is shifted to
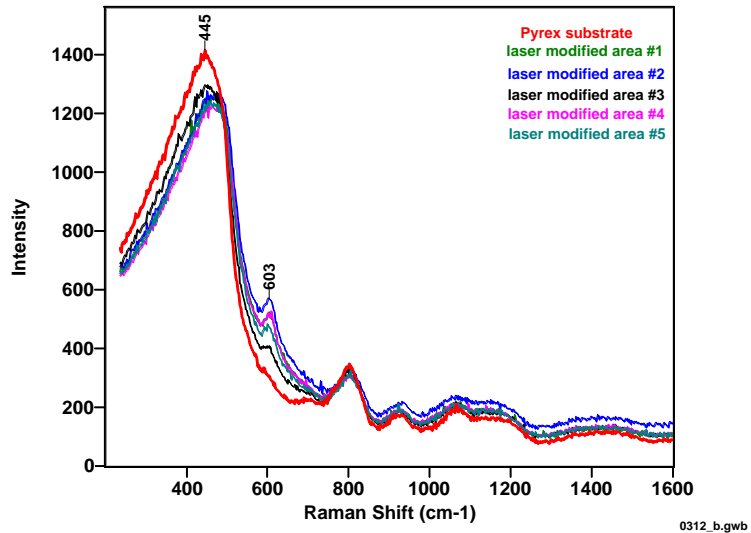
Fig. B3.2.4 Raman spectra of Pyrex glass. A comparison between unmodified (red) and laser modified areas.

high frequency, and a Raman band peaking near 603 cm^{-1} appears for laser-modified regions. The upward shift in the 445 cm^{-1} band indicates the formation of 4-membered silica rings, and the appearance of the 603 cm^{-1} band indicates the formation of 3-membered silica rings, respectively. Furthermore, an enhanced Rayleigh scattering of the laser beam in the laser-modified regions during Raman study was observed, an indication of a difference in refractive index between modified and unmodified regions. The formation of 3- and 4- membered rings by the fs laser pulses, as well as a slight reduction in the overall intensity of the Raman bands are also observed in CVD quartz with laser energy below the photo-damage threshold. In contrast to the photo-damaged area, the narrowing of the Raman band peaking between 400 and 500 cm^{-1} is not observed in the laser-modified regions.

To understand the effect of structure modification by fs laser pulses in the embedded waveguide regions (below the photo-damage threshold), laser-modified dots with 5,000 accumulated pulses were created with different pulse energy for a Raman spectrometer study. The laser-modified regions are the six patterns of four dots (viewed end-on) in a square, each square corresponding to a different pulse energy (0.90, 0.81, 0.72, 0.63, 0.54, and 0.45 µJ/pulse), as shown in the insert image from upper left to lower

right in Fig. B3.2.5. These dots, as shown in the previous section, possess optical birefringence and are bright in transmitted light with crossed polarizers. Laser illumination of these modified regions for Raman analysis resulted in enhanced Rayleigh scattering of the laser beam, which is an

Fig. B3.2.5 Factors from discrimination analysis of Raman spectra from laser modified and unmodified regions of the square-dot silica glass (insert shows the square-dot pattern)

indication of a difference in refractive index. The Raman spectra on each of the dots (in the end-on orientation) and on nearby, unmodified regions of the quartz glass were obtained (a total of 48 spectra). The spectra from the dots appear, on average, to have slightly less intense Raman features than those from the unmodified areas. In addition, there appear to be subtle differences between the Raman bands from the dots and the unmodified regions over the frequency range (400-600 cm^{-1}) associated with small silica rings. A multivariate, chemometric analysis[47] on these spectra was performed to better distinguish these subtle differences. Using matrix algebra, this analysis simultaneously processed all 48 spectra in the set. This analysis looks for differences between spectra and generates a set of factors. These factors look like spectra and may be thought of as components of the experimental spectra. One important characteristic of the factors is that parameters used to scale the factors are called "scores". A score can be thought of as the relative contribution of a factor to one of the experimental spectra. Thus, the discrimination analysis generates one set of spectra-like factors for the entire set of experimental spectra but generates a separate set of scores (one for each factor) for each experimental spectrum.

Fig. B3.2.5 plots the first four factors from the discrimination analysis of the 48 spectra. Factor 1 (illustrated by blue) is the average spectrum of all the experimental spectra employed in the discrimination analysis. High-numbered factors are added to factor 1 to reproduce the experimental spectra. Factor 2
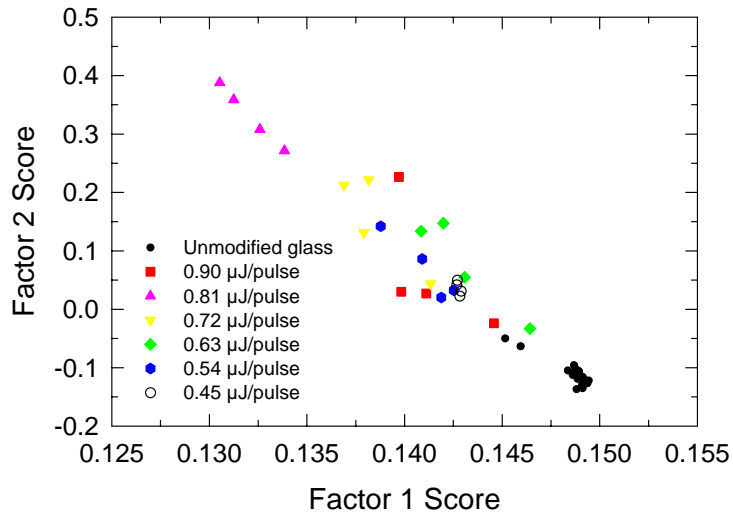
Fig. B3.2.6 A plot of scores of factor 2 versus the scores of factor 1. Each point corresponds to one of the spectra from modified and unmodified regions.

(presented by red) is significantly more intense than factor 3 and 4, which are more intense than even higher-numbered factors (not shown). Factor 2, therefore, represents what is probably the most significant difference between the experimental spectra. Fig. B3.2.6 plots the scores for factors 1 and 2 from the discrimination analysis of Raman spectra from the laser modified and unmodified regions of the square-dot silica sample. Clustering of data points in Fig. B3.2.6 means that the spectra corresponding to the points in the cluster have similar contributions from factor 1 and factor 2. Separation of data points means the corresponding spectra have different contributions from factors 1 and 2. The data point for the unmodified regions are clustered at the lower right of the plot. In fact, all the unmodified (amorphous silica) data points have lower factor 2 scores than any of the modified data points. This indicates that the spectra from laser-modified regions have higher contributions from factor 2, at the expense of their contribution from factor 1, than the spectra from the unmodified regions. Of the spectra from modified regions, those resulting from modification with a pulse energy of 0.81 µJ have the most factor 2, followed by the 0.72-µJ dots. The 0.90-µJ, 0.63-µJ, 0.54-µJ, and 0.45-µJ dots have less factor 2 than the 90-µJ and 80-µJ dots but more than the unmodified glass regions.

Factor 2 (in Fig. B3.2.5) shows two prominent, positive features, one peaking at 512 cm^{-1} and one peaking at 610 cm^{-1}, plus a negative-pointing feature near 487 cm^{-1}. Positive-pointing features represent species that are more prevalent in spectra with higher factor two scores (like the modified regions) and vice-versa for the negative-pointing feature. The 610 cm^{-1} feature corresponds to 3-membered silica rings. The Raman feature for the 4-membered silica ring occurs near 495 cm^{-1}. The up-shift of the 4-membered silica ring to 512 cm^{-1} suggests that these 4-membered rings are under compressive stress. Therefore, the scores for factor 2 indicate enhanced concentrations in the laser modified regions with 3- and 4-membered silica rings, with some 4-membered rings created from unstrained precursors (see the negative-pointing 487 cm^{-1} feature in factor 2, Fig. B3.2.5). These small rings may be forming at quasi-surfaces on small, perhaps nanoscale, voids regions associated with laser modification regions in glass.

Factor 3 and factor 4, unlike factor 2, do not discriminate between the spectra from the laser-modified and the unmodified regions. However, both the spectra form the 0.45-µJ dots and nearby unmodified regions show enhanced contribution from factor 4 (not shown). Factor 4 (when its plot is expanded to study it in detail) appears to correspond to variations in the amounts of 5-, 6- and 7-membered rings (the broad band peak near 450 cm^{-1}, Fig. B3.2.2). There is probably a small variation in bulk glass structure near where the 0.45-µJ modified regions were formed.

In summary, these Raman studies have revealed that intense femtosecond laser pulses can reduce the population of large network ring structure in the glass and increase the number of 4- and 3-membered silica ring structures in glass. With the formation of these small network ring configurations, laser modified glass region can be compacted more efficiently in comparison to the bulk glass. Furthermore, the observation of an up-shift of the Raman band for the 4-membered silica rings from 490 cm^{-1} to above 512 cm^{-1} suggests these rings are under compressive stress. [17, 48] These observations indicate that local densification could contribute to the increase of refractive index in the laser modified regions in glass.

B3.3 Laser Induced Birefringence in Optically Isotropic Glass

Figure B3.3.1 (a) shows a transmission image (through z, or laser beam direction) of femtosecond laser modified regions in a CVD quartz plate between two crossed polarizers. Each modified region was exposed to 60,000 pulses (1 minute dwell time) parallel to the beam direction with average pulse energy of 0.9 µJ. The glass plate was then rotated 10° after each laser irradiation. Since the amorphous quartz plate is optically isotropic, the bulk glass is dark when two polarizers are crossed. The laser-modified regions (as shown by the spotted ring configuration), however, are bright, indicating the creation of birefringence in these regions. Fig. B3.3.1 (b) illustrates the transmission variation of these modified spots in the first quarter of the ring structure. Results indicate that the intensity of transmission changes sinusoidally. It is well known that the transmission through the second polarization analyzer depends on the amount of phase retardation
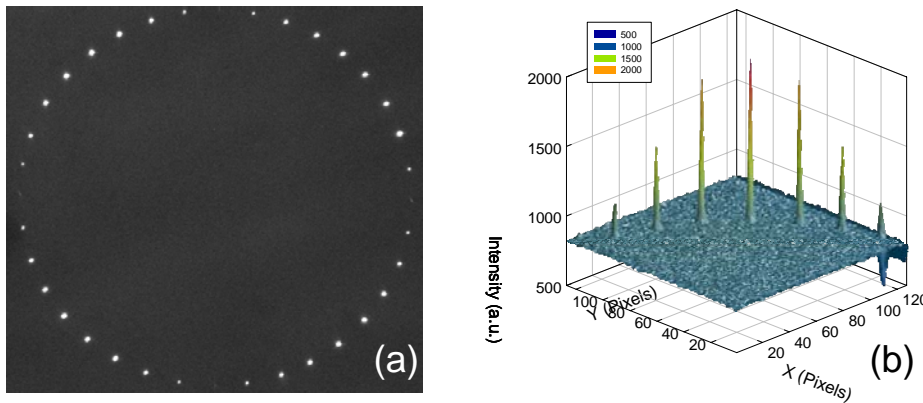
Fig. B3.3.1 (a) The transmission image of laser modified regions under a cross-polarized light condition, the polarization direction of each modified region is rotated 10°, (b) the change of transmitted light intensity in the first quarter of the circle.

($\Delta\varphi = 2\pi(n_e - n_o)d/\lambda = 2\pi\Delta nd/\lambda$, d is the thickness of the birefringent medium) and the orientation angle (θ) of the birefringent optical axes (see Equation (3)). Since the amount of phase retardation created by the femtosecond laser pulses remains the same for these spots, the sinusoidal change in the transmission from spot to spot indicates that the optical axes of the birefringent medium has been rotated by the polarization change of the writing laser. Since the polarization direction of the laser beam is rotated $10°$ from spot to spot, there should be a direct correlation between the polarization direction of the writing laser and the orientation of optical axes of the laser modified birefringent

medium. This correlation is immediately confirmed when the transmitted light becomes extinct (see Fig. B3.3.1 (a)) every 90°. These observations prove that the optical axis of femtosecond laser induced birefringence in bulk glass can be controlled by the polarization direction of the femtosecond writing laser.

For a transparent optical birefringent medium between two-crossed polarizers, the optical transmission (T) is,

$$T = \frac{1}{2}\sin^2(2\theta)[1 - \cos(\Delta nkd)] \qquad (3)$$

where $\Delta n = n_e - n_o$, k = 2 / , and d is the thickness of the birefringent region through which the light travels. As a first order approximation, we assume the laser-induced birefringence is proportional to the intensity of light[49]. Therefore, the induced birefringence along the z-axis (x, y =0) for a focused Gaussian beam is,

$$\Delta n = \frac{\Delta n_o}{1 + (\frac{z}{z_o})^2} , \qquad (4)$$

z_o is the Rayleigh length and Δn_o is the peak value of the birefringence.

Overall optical path delay (or the total retardation Δ) for two polarizations is

$$\Delta nd = \int_{-\infty}^{\infty} \frac{\Delta n_o}{1 + (\frac{z}{z_o})^2} dz = \pi \Delta n_o z_o \qquad (5)$$

where $z_o = \pi \frac{w_o^2}{\lambda}$, is the wavelength in glass, and w_o is the waist of the Gaussian beam. Substituting Eq. (5) into Eq (3), the transmission through the sample and second polarization analyzer can be determined by

$$T = \frac{1}{2}\sin^2(2\theta)[1 - \cos(\pi \Delta n_o kz_o)] \qquad (6)$$

Based on Eq. (6), the transmission through a birefringent medium between two-crossed polarizers depends on the value of the birefringence, the wavelength of the probing light, the thickness of the birefringent material, and the angle between ordinary direction of the birefringent material and
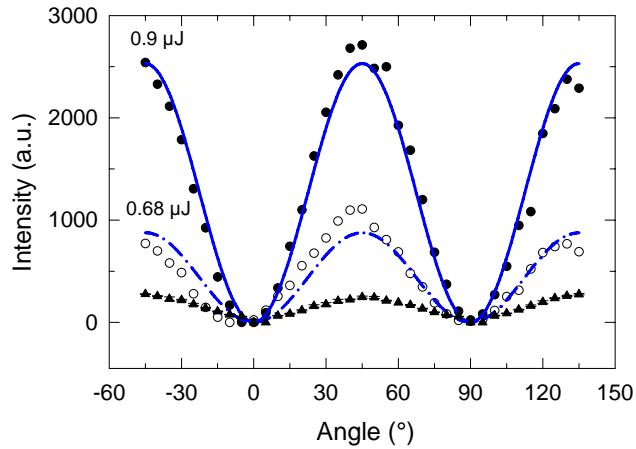
Fig. B3.3.2 Variation of the transmitted light intensity as a function of sample orientation.

polarization axis of the first polarizer. Fig. B3.3.2 illustrates the variation of transmission as a function of sample rotation angle between two-crossed polarizers. The open circle and solid circle represent the changes of transmitted light intensity for regions that have been exposed to the 0.68 µJ and 0.90 µJ pulses for 10 minutes under white light illumination, respectively. The dotted and solid lines are the curve fitting results based on Eq. (6). Results show that the laser-induced birefringence is greater for the region exposed to the higher energy pulses than the region exposed to the lower energy pulses. The average intensity and standard deviation from four measurements collected for the monochromatic light (at 671 nm) are shown by the triangles. The measurement was performed on a region where the glass has been exposed to the 0.9 µJ pulse for 4 minutes. The introduction of the light band pass filter significantly reduces the total light intensity through the bottom polarizer and results in lower intensity variation. However, the general behavior is consistent with the predicted behavior of an optical birefringent medium.

Direct observation using an optical microscope under two-crossed polarizers gives the spot size of the laser-modified region in the bulk glass. The diameter of the laser-modified spot is about 3 µm and the average thickness of these birefringence regions is about 25 µm. The calculated thickness of the modified regions, based on twice of the Rayleigh length ($2z_o = 2\pi w_o^2/\lambda_i$; $\lambda_i = 548.7$ nm in amorphous quartz) is about 25.8 µm, which is consistent with experimental observation. Furthermore, it is found that

perpendicular to the writing laser propagation direction, these modified regions also show the extinction behavior between two-crossed polarizers for every 90° rotation, suggesting that the laser-modified regions possess a biaxial optical birefringence.

From Eq. (6), the laser-induced birefringence (the peak at the center of the spot) can be obtained by measuring the transmission at the condition of θ = 45° with the assumption that the laser modified birefringent region has a fixed depth of twice the Rayleigh length (25.8 µm). Fig. B3.3.3 shows the maximum change of birefringence (Δn_o) induced by the laser as a function
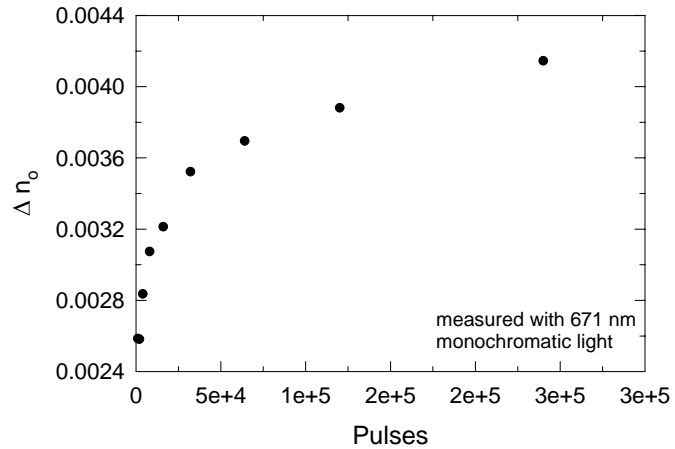
Fig. B3.3.3 Change of laser-induced birefringence in bulk silica as a function of the number of accumulated laser pulses.

of the number of laser pulses. Results show that the maximum change of birefringence increases rapidly at the beginning then starts to level off as the number of laser pulses increases. This phenomenon is similar to the experimental observation using a polarized excimer laser source.[6] However, under the excimer laser irradiation laser energy is linearly absorbed only near the surface of the glass, while under the femtosecond laser irradiation photon energy can only be absorbed through a nonlinear process where a threshold intensity is required for the multiphoton absorption to occur.

Although the fundamental mechanisms creating the birefringence in the bulk glass by the femtosecond laser irradiation are not clear yet, several observations in this investigation have helped to shed light on this issue. Our results show two interesting phenomena including (1) the high energy linearly polarized laser pulse can induce birefringence in optically isotropic glasses, (2) the optical axes of the birefringence depend on the polarization direction of the laser beam. The polarization dependence of birefringence immediately suggests that the optical birefringence cannot be solely attributed to a thermal effect generated by multiphoton absorption. If the localized thermal heating is a major contributor, the laser-modified region should be optically

isotropic. It is well know that glasses can be poled under ultraviolet light[6,50] or high dc bias condition at high temperature[51] to create nonlinear optical behavior. Furthermore, recent investigation[52] on the local atomic structural change by an in-situ laser irradiation has demonstrated a polarization-dependent structure change in

Fig B3.3.4 The development of microcracks due to a laser-induced tensile stress between laser-damaged lines (25 µm separation).

amorphous chalcogenide glasses. Polarization direction of the femtosecond laser also plays an important role on the shape of holes drilled during micromachining of metals.[53] The field or polarization dependence mechanism is especially applicable to the femtosecond laser processing since the estimated optical field generated by the femtosecond pulse is on the order of 10^{11} V/m. This strong electrical field can effectively induced an anisotropic contraction by an electrostrictive effect.[54] The electrostrictively induced strain will put a tensile stress between two parallel waveguides or laser damged

lines. Fig. B3.3.4 shows a high density laser-damaged pattern (25 µm separation of laser direct-written lines). Note the direction of microcracking generated by a laser direct-write process, where cracks propagate parallel but are not attracted to laser-written lines (lines in this case). This observation suggests that a compressive stress generated by the electrostrictive effect in the laser-modified regions creates a tensile stress between the
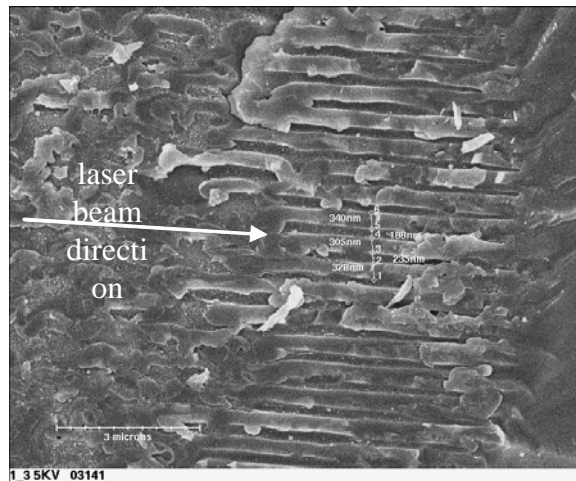
Fig. B3.3.5 SEM microphotograph of photo-damaged region on a three-point bend fracture surface (arrow indicates the laser beam direction).

lines, which opens up cracks perpendicular to the tensile stress direction.

Following this optical field-induced deformation with an immense localized heating and rapid quenching, the overall effect could result in an irreversible electrostrictive deformation and create an anisotropic densification that is analogous to the mechanism proposed for ultraviolet-induced densification[27] of fused silica. Fig. B3.3.5 shows a microphotograph of a scanning electron microscopy (SEM) image of the photo-damaged region inside the glass through
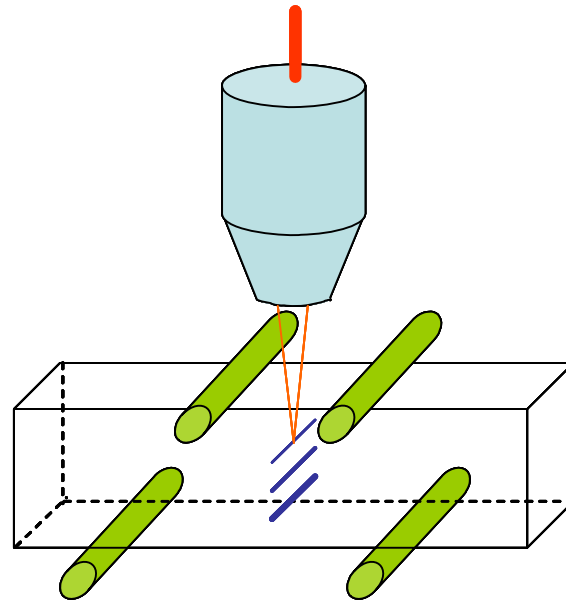
Fig. B3.3.6 Experimental setup to obtain microstructure of laser-damaged areas through a three-point fracture.

fracture. Fracture surfaces that exposed the damaged areas were obtained through a three-point bending experiment, where several photo-damaged waveguides written with pulse energy greater than 25 µJ were aligned at the center of the glass bend bar (where it had a maximum bending moment, see schematic illustration on Fig. B3.3.6). A periodic nano-scale structure consisting of thin parallel glass plates and voids in the damaged areas was observed by SEM (Fig. B.3.3.5), where the laser-induced periodic structure is perpendicular to the laser polarization direction. The creation of this periodic structure perpendicular to the laser propagation direction suggests an anisotropic contraction in the field direction. As this anisotropic contraction along the field direction increases with increased pulse energy, a periodic structure with a denser glass and void
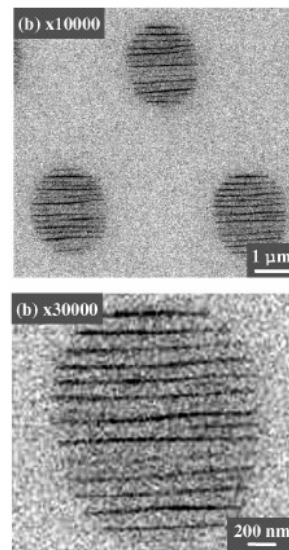
Fig. B3.3.7 Backscattering electron images of laser-modified region at focus spot (Y. Shimotsuma et. al).

is created to satisfy conservation of mass. More interestingly, the periodicity of the laser induced nano-structure (~ 540 nm) is close to the wavelength of the incident laser (800 nm) traveling in silica (548.7 nm). Difficulties were experienced in identifying such period structures in laser modified region in glass when pulse energy is below the damage threshold (< 0.9 µJ/pulse). However, the observation of fs laser-induced nano-scale periodic structure in fused silica at 1 µJ/pulse was recently reported in the literature (see Fig. B3.3.7).[55] An increase in these nano-scale, periodic structures by fs laser pulses will increase the light scattering loss in waveguides, which is consistent with experimental observations presented in a later section (section B 3.3.2). In addition, the formation of quasi-surface at laser damaged region is also consistent with previous Raman study, where overall Raman intensity decreases and the intensities of smaller planar rings increase (section B3.2.2). It is believed that the laser-induced periodic structure with different refractive indices could also contribute to the development of optical birefringence in bulk glass. Birefringence of this nature is well known as "form" birefringence, [56] where birefringent properties can be created by a periodic ordered structure (or particles) whose periodicity is small compared with the wavelength of probing light (650 nm in this study).

B3.4 Laser Direct-Write Embedded Waveguides and Integrated Optics

B3.4.1 Processing Condition verse Transmission Mode

With the knowledge of the effect of average laser power (section B3.1) on structure modification of glass, direct-writing waveguides inside amorphous quartz was explored. Figure B3.4.1 shows the top view, near-field and far-field patterns of laser-modified waveguides above (0.1 mJ) and below photo-damage threshold (0.9 µJ) in thermally treated CVD quartz. The near-field and far-field patterns were obtained from the transmitted beams at 650 nm through 2 mm length of laser-modified regions. The near-field pattern of waveguides created below the damage threshold (bottom images) illustrates the propagation of a single LP_{01} mode through the waveguide inside of a bulk glass. The far-field pattern indicates that this transmitted mode possesses a nearly Gaussian profile. Above the damage threshold (top images), no far-field patterns can be obtained due to a significant transmission loss in the waveguides.

The transmission loss determined from the top view is summarized in Figure B3.4.1. Above the photo-damage threshold (> 0.9 µJ), extensive light scattering is observed, which is consistent with the Raman analysis results where some glass has been partially replaced by voids. Results also show that below the photo-damage threshold, the transmission loss is almost negligible within 2 mm. These embedded waveguides in the amorphous quartz are preserved after a half hour thermal treatment at 650°C, indicating a permanent change of refractive index created by the fs laser pulses.
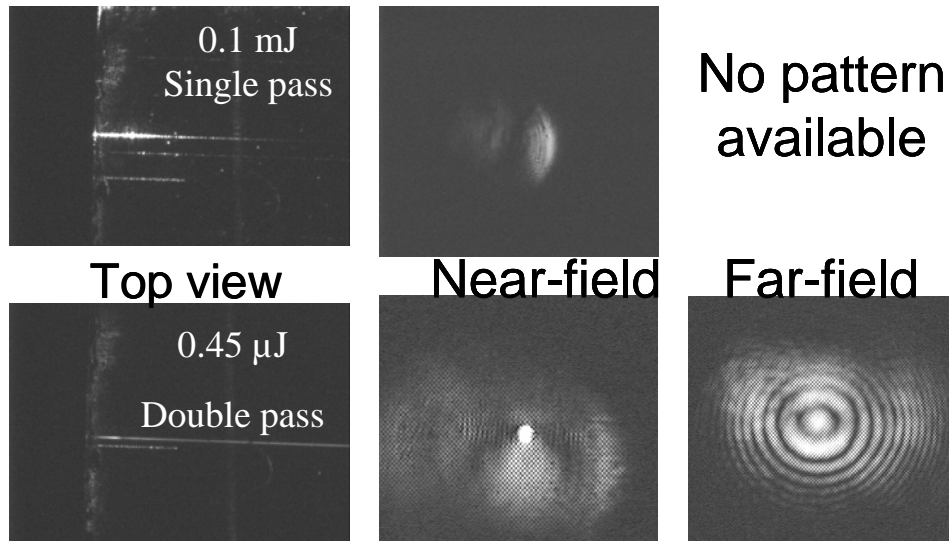
Fig. B3.4.1 Direct-write embedded waveguides in glass by femtosecond laser pulses. The top and bottom images are regions modified above and below photo-damage threshold, respectively.

Fig B3.4.2 illustrates the changes of transmission mode for laser direct-write waveguides in amorphous silica as a function of processing conditions. Light from a laser source (λ = 650 nm) was coupled into the waveguide through a focusing lens, and the near-field intensity distribution of the guided mode was obtained by imaging the backside of the fabricated waveguide onto a CCD camera. By carefully aligning the axis of the input laser and the orientation of the waveguide (~ 3 µm in diameter), a single mode (TEM_{00}) can be excited in the waveguides fabricated with a pulse energy of 0.45 µJ. This single guided mode with a near Gaussian profile is demonstrated by a 3D field intensity distribution on the insert of Fig. B3.4.2. However, when the number of passes increases (as shown in the X axis) or the pulse energy increases (in the Y axis), a higher-order mode (TEM_{01}) is developed in these waveguides. Finally, when the pulse energy

exceeds the photo-damage threshold, high-order, multiple-mode (TEM_{11}) is observed. Furthermore, most of the light was scattered through propagation, and the damaged waveguides did not efficiently guide light.[17] It is well known that increasing the average laser power can enlarge the laser-modified region[57] and increasing the number of accumulated laser pulses can enhance the refractive index change[58] in the glass. The combination of creating waveguides with a larger diameter and a higher refractive index change alters the transmission property from a single guided mode to high-order, multiple modes. Similar results have also been reported by changing the writing speed, where decreasing writing speed switches the guided mode from a single fundamental mode to higher order modes.[59]
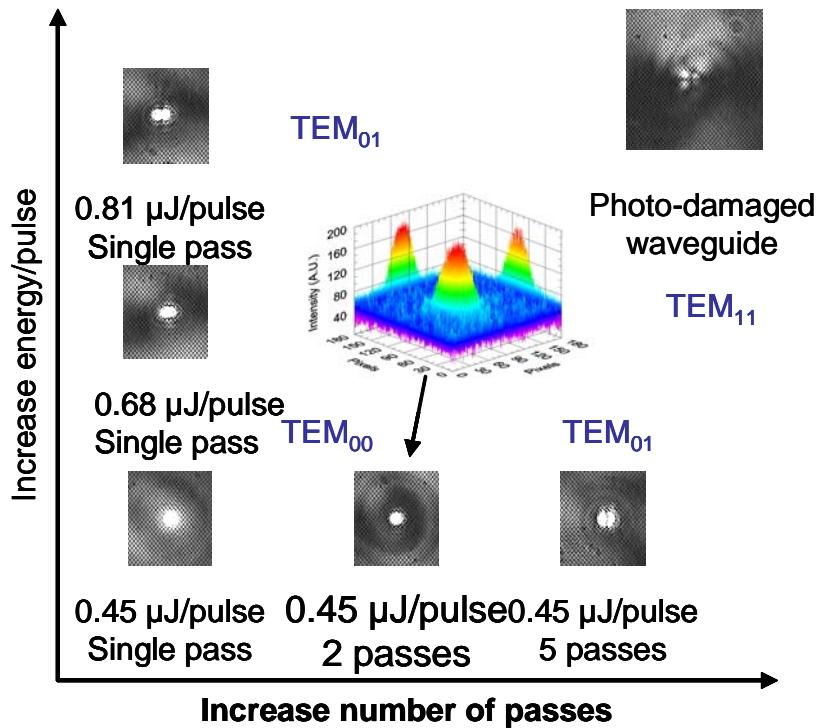
Fig.B3.4.2 Processing condition versus transmission mode of laser direct-written waveguides, measured by near-field images.

B3.4.2 Processing Condition, Refractive Index Change, and Optical Loss

      The control of transmission loss in the waveguides is important for practical applications, and is extremely sensitive to the fabrication process, glass composition, and defects in the optical medium.   For a straight waveguide, the majority of the loss can be

attributed to light absorption by the material and light scattering from defects along the light propagation direction. The overall transmission loss can be determined by the amount of light scattering along the propagation direction, by measuring the light intensity variation perpendicular to the writing direction. High quality waveguides will show small or

Fig. B3.4.3 The light scattering (intensity change from a top view measurement) in the waveguide along the propagation direction.

undetectable intensity variations along the light transmission direction. Fig. B3.4.3 illustrates the light intensity changes (due to scattering) along the transmission direction in laser direct-written waveguides as a function of pulse energy, after light was first coupled into these waveguides and followed by self mode adjusting. These straight lines are obtained from a linear fitting of light intensity with respect to the propagation distance. Results show that waveguides fabricated with higher pulse energy have stronger light scattering and quick intensity decay along the transmission direction (as indicated by the negative slope change). The losses in these waveguides, based on the light scattering measurement (with light source at 650 nm), vary from 0.36 dB/cm to 3.59 dB/cm as pulse energy increases from 0.45 to 0.81 µJ/pulse. However, the transmission

loss determined by the near-field intensity for waveguides (fabricated at 0.45 µJ/pulse) of different lengths is about 1.13 dB/cm, which is similar to data in the literature.[20]

The change of refractive index between the laser modified core region and surrounding glass can be roughly estimated from the numerical aperture (NA) of the fabricated waveguide by a
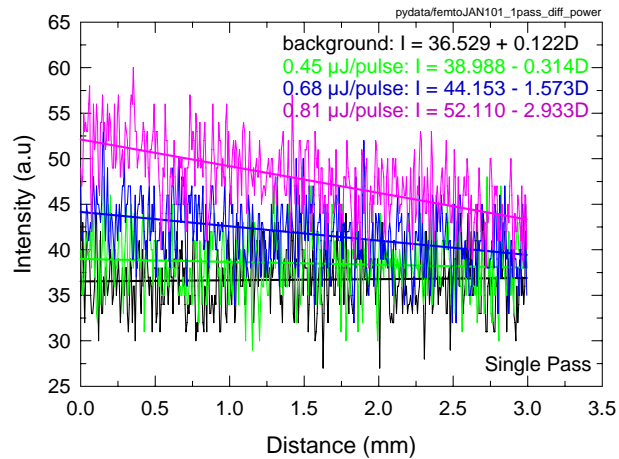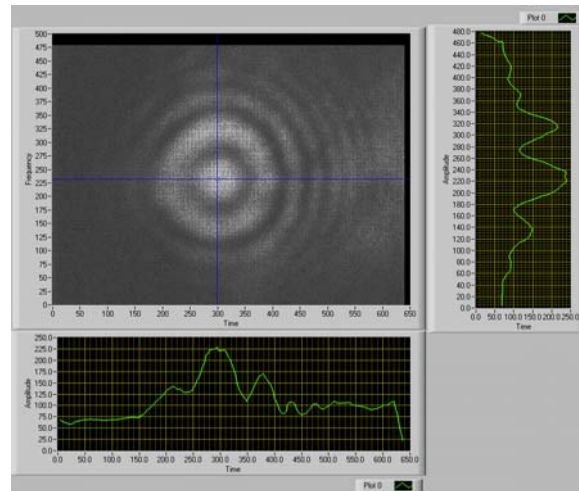

Fig.B3.4.4 Using the onset of the double-lobed far-field pattern to estimate the refractive index change from a laser direct written waveguide in bulk glass.

far-field measurement ($\Delta n = 2\pi r NA/\lambda$) at the appearance of the second mode. The estimated value for the refractive index change measured at the onset of the double-lobed far-field pattern (see Fig. B3.4.4, with a radius of r) with pulse energy at 0.45 µJ/pulse is about 1.34 – 1.57 X 10^{-4}, assuming a simple step-index waveguide. Although a higher refractive index change can be produced with increased pulse energy, the transmission properties of the waveguide will be forfeited. As a result, the following optical devices were made at the pulse energy of 0.45 µJ.

B3.4.3 Direct-Write Integrated Optics

The use of integrated optics for sensing applications is receiving increasing attention. Integrated optics offer high-information-carrying capacity, small size and weight, immunity to electromagnetic interference, and unparalleled signal security. The new capability to fabricate waveguides inside of amorphous silica by femtosecond laser pulses has fueled a major thrust to explore this technology for device fabrication. This approach simplifies the manufacturing process and provides greater flexibility compared to conventional waveguide fabrication processes.[60,61] A variety of devices, such as waveguides[3, 4, 14, 17, 19, 20], gratings[62], couplers[63], splitters[5], micro-mirrors[64], and photonic structures[7] have already been realized using this method. Several prototype devices fabricated by the femtosecond laser direct-write technique are presented. The construction of these devices relies on the ability to create low loss, single mode waveguides in the bulk glass. These results demonstrate that direct-writing of embedded waveguides by femtosecond laser pulses is a promising approach to fabricate integrated optics.

B3.4.3.a Y coupler

Fig. B3.4.5 shows the intensity variation of the outputs in a photo-written Y coupler, based on the schematic layout in the insert. The written pattern has a 2° bend on each
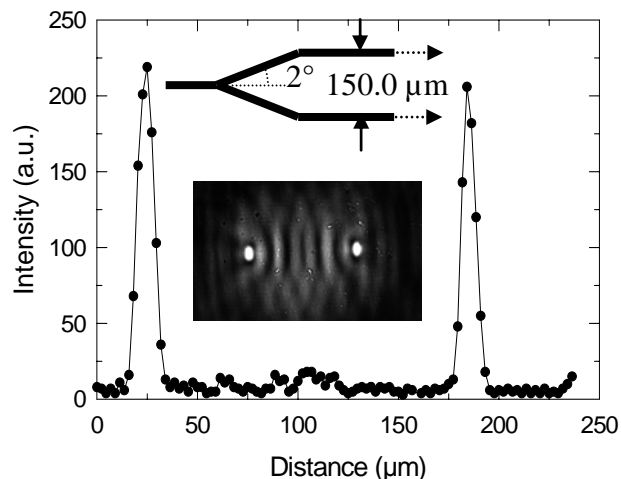
Fig. B3.4.5 The output intensity of a Y coupler

arm and a 155 µm separation. Using a pulse energy of 0.45 µJ and a writing speed of 20 µm/sec, the intensity of outputs from each arm in this Y coupler is almost equally divided (50/50 splitting). The image of the output (see the insert image) shows high intensity spots at the end of each waveguide and a weak interference pattern between these two arms.   The output intensity was found to be strongly dependent on the bending angle. Results indicated that when the bending angle increased to 10° hardly any light can be efficiently transmitted through this bending configuration. Evidence has shown when replacing the straight-bend configuration with a 5 cm curvature bending on each arm, the splitting loss of the Y coupler can be significantly reduced.

B3.4.3.b Directional coupler:

Fig. B3.4.6 illustrates the output intensity differences between a long bent waveguide and a coupled waveguide. The schematic of this directional coupler is shown on the right hand side of the figure. The coupling property was studied by focusing a 650 nm laser beam into the long waveguide and guided through two 2° bends and observing the near-field pattern of the coupler's output.   The output of
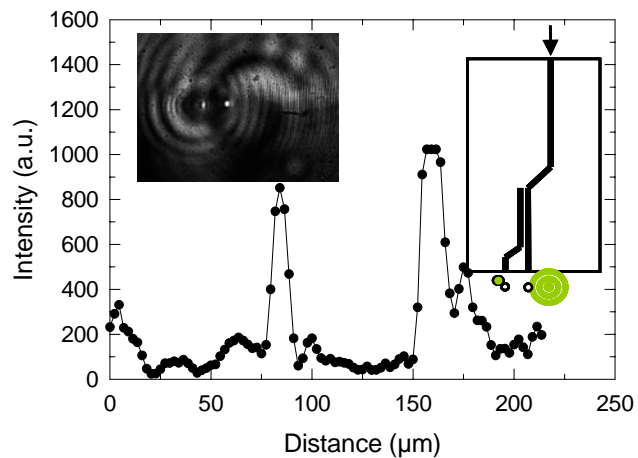
Fig. B3.4.6 The output intensity of a directional coupler. The intensity of the launching waveguide is saturated.

this launching waveguide is shown as the brightest spot on the image (see inserted image), with an intensity that saturated the light detector (as shown by a flat top on Fig. B3.4.6). Along the straight launching direction, a far field pattern was generated. A weak, yet distinct light spot can also be observed to the left of the brightest spot in this image. This spot represents the light intensity created by an electromagnetic coupling through a 3 µm gap between the launching and coupled waveguides. The shape of these spots is indicative of single-mode propagation.

B3.4.3.c Mach-Zehnder interferometer

Fig. B.3.4.7 shows the changes of output intensity of an equal path-length Mach-Zehnder interferometer as a function of time (t_o to t_4 as time increases) when one arm of the interferometer was heated by a soldering iron. The schematic of the directly written optical interferometer is inserted on the top of the figure. Local heating generated from the soldering iron changes the refractive index of the waveguide and creates a phase shift between two arms, which alters the intensity of interference pattern. Therefore, as glass temperature near the soldering iron progressively increases, the amount of phase shift increases and the overall output intensity due to interference from both arms decreases.
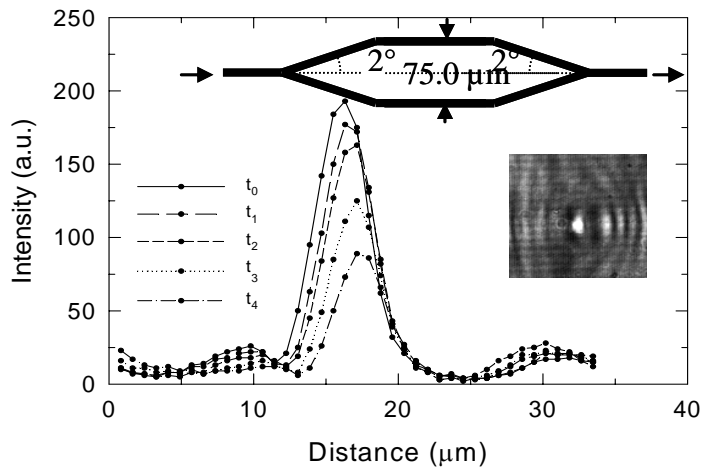
Fig. B3.4.7 Progressive change of the interference intensity output as one of the arms in this interferometer is heated.

B3.5 Laser Micromachining of Sub-Surface Micro-Channels

The use of micro-channels in the micro-fluidic MEM (micro-electro-mechanical) devices has gained much attention for chemical sensing (such as chem-lab on a chip) or controlled chemical reaction (micro-reactors), and many of which have important implications to our national security. Fabrication of these sealed micro-channels in glass is quite complicated, including photo-delineation of channel pattern, magnetron assisted plasma etching, as well as lamination and hermetic sealing. These processes rely heavily on advanced processing equipment which is both capital and maintenance intensive. In addition, only surface features can be fabricated. Embedded 3D micro-channel fabricated by the femtosecond direct-write technique was recently demonstrated in the literature. The approach provides a simple and promising solution to fabricate sub-surface micro-

channels without an additional sealing process. Two different approaches have been developed including, (1) laser assisted direct ablation and (2) laser patterning and developing for a photosensitive Foturan glass (Schott glass). For both processes, multi-photon absorption associated with the ultrashort laser pulse is the enabling process to locally alter or ablate the glass and to create 3D structures inside of a bulk glass. The first process, assisted by the high energy photons generated at the laser focus point in the water (due to a continuum white light generation), ablates the glass and directly creates a channel as the focus point moves from rear side into the glass. This approach can be used for glass of different compositions. However, the diameter of ablated channels is extremely small (< 5 µm) and the side wall is ragged. The second approach, similar to a space-selective crystal growth technique, produces crystalline seeds at the laser focus point though a photochemical reaction in the amorphous glass matrix. After moving the focus spot inside of a glass in delineating the desired channel pattern, only these seeds in laser modified regions will grow into a crystalline phase in a subsequent thermal process, and the crystalline phase eventually will be selectively etched away in a dilute HF solution, leaving micro-channels in the glass matrix. The selective etching during the developing process produces large diameter channels (> 50 µm) and smooth side walls. In addition, microstructuring of movable parts in a large embedded chamber has been demonstrated for pumping fluid in a Foturan glass. Inspired by these exciting developments and an untapped potential for the integration of direct-write micro-fluidic and integrated optic sensing system (such as the Mach-Zehnder interferometer in section B 3.4.3.c), we have explored the femtosecond laser microfabrication effort for micromachining sub-surface micro-channels in Foturan glass.

B3.5.1 Experimental Procedure

Pulse energy in producing crystalline seeds in Foturan glass was varied to determine the processing window. No attempt was made to identify the lowest processing window in this preliminary study. It was found that pulse energy in the range of 25 µJ to 100 µJ would effectively produce a desirable channel pattern without generating laser damage on the glass surface. Therefore, the pulse energy required to

create crystalline seeds Foturan glass was much greater than it was required for fabrication optical waveguides in a bulk glass. Embedded channels were successfully fabricated by moving the focus point at 500 µm below the glass surface with transverse writing speed varied from 500 µm/sec to 2,000 µm/sec. After the channel patterning is defined, the glass sample was heated in a furnace at 5°C per minute to 500 °C and held for one hour to produce effective nucleation sites for a later growing process at 605°C.

From 500°C to 605°C, sample was heated at 3°C per minute. The seeded crystalline phase continued to grow at 605°C for one hour. After the completion of the nucleation and growth process, the sample was furnace cooled to room temperature. The laser defined pattern can now clearly be seen due to a change of color (exposed region turned to a yellow-orange color) by the re-crystallization process. The sample was then put in a dilute HF solution (10 vol. %) at 75°C to selectively etch the crystalline phase and develop the channel pattern in the Foturan glass. A good etching selectivity between the crystalline phase and the amorphous Foturan glass matrix produced well defined embedded microchannels in the glass. It was found that additional ultrasonic assistance would help the developing process. The features of the developed channel and wall were studied by scanning electron microscopy.
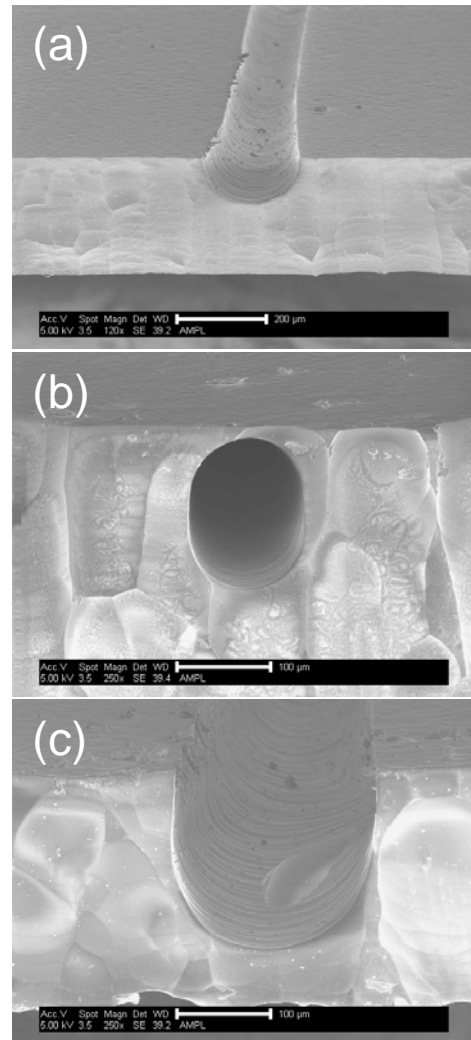

Fig B3.5.1 Micro-features created by femtosecond laser micro-fabrication. (a) surface trench, (b) embedded chanel, and (c) trench with vertical walls on both sides. (Details see text).

B3.5.2 Micromachining of Foturan Glass

Fig. B3.5.1 (a) shows a round bottom trench fabricated on the surface of a Foturan glass sample, where the laser beam was focused at

250µm below the glass surface. The edges and wall on the trench created by the patterning and developing process are smooth and well defined, indicating a superior feature of this approach in comparison with the laser ablation process. It is believed that a higher index of refraction of the Foturan glass brought the focus point closer to the glass surface. Etching the embedded channel near glass surface opened up the channel and produced trenches on the surface. This argument is supported by a wider opening of the trenches near the edge of the glass where HF solution produced excess etching at the initial entrance of the embedded channel. The widening of the entrance point is also a common feature for the embedded channels.

It was found that the width and depth of the trench depends on the pulse energy. Higher pulse energy produced wider and deeper trenches, suggesting more seed crystals were produced by the photochemical reaction during the patterning process. Fig. B3.5.1 (b) illustrates an embedded channel fabricated by this technique, where the laser was focused at 500µm below the glass surface. The channel has a wide openning at the entrance and tapered in as less etchant could move into the embedded channel (or inside of the glass). It is found that these channels possessed an elongated round geometry, presumably as a result of the laser profile when the focus spot was moving transversely to the beam direction. The elongated shape can help to create an almost vertical wall for a surface trench as it is shown in Fig. B3.5.1 (c). Although the overall process has not yet been optimized, the preliminary results have demonstrated the potential for fabricating integrated optical and micro-fluidic systems for sensing applications.

B4. CLOSING REMARKS

The research work has investigated the effects of glass compositions and laser processing conditions on the optical properties and performance of embedded optical waveguides fabricated by the femtosecond laser direct-write approach. Based on the Raman spectroscopy, femtosecond laser pulses modified the local silica network and created smaller planer rings and narrowed the distribution of large silica rings, which could contribute to the increase in local density and index of refraction.   Results showed waveguides can be readily created and retained in glasses with high glass formers

(such as silicon and boron). Glasses with a high concentration of modifiers tend to create color centers, photo-damages, and the local structural modified by the laser can be easily removed by an addition heat treatment. Results showed that there was a tight operational window (0.45 to 0.90 µJ/pulse) to create functional waveguides without causing significant optical loss due to photo-damages. The fabrication of embedded low loss waveguides with a single transmission mode was demonstrated. High pulse energy and repetitive writing generated multiple transmission waveguide modes, due to the increase in waveguide diameter and local index refraction. Using an optimal processing condition, several prototypes of integrated optics such as Y coupler, directional coupler, and Mach-Zehnder interferometer were fabricated with promising performance. These results demonstrate the quality of the waveguides and simplicity of this direct-write approach. Furthermore, an unusual laser-induced birefringence in an optically isotropic bulk glass was observed. We were among the first few groups in the world to observe such an unusual behavior, and were the first to quantitatively verify this phenomenon and correlate the observed birefringent property to the polarization direction of the laser beam. Experimental results show that the optical axes of laser-induced birefringence can be controlled by the polarization direction of the femtosecond laser. In addition, the effects of processing condition on the changes of birefringent properties induced by the femtosecond laser pulses were also documented. Data indicates that the change of laser-induced birefringence depended on the number of accumulated pulses and pulse energy. Experimental observations that might contribute to the basic mechanisms generating this unusual behavior were reported. The need to enhance the local refractive index change and to minimize the transmission loss were identified as key issues for further advancing this technology into integrated systems. The feasibility of using a femtosecond laser to create embedded channels in bulk glass was explored and demonstrated.

This work demonstrates that femtosecond laser direct-write is a promising technology to fabrication 3D waveguides and integrated optics in bulk glass. The approach together with newly developed direct-write 3D microstructuring has become a critical emergent technology for microfabrication of integrated optical microsensing systems. The potential to create a periodic photonic structure in bulk glass by the direct-

write laser technology for band gap control applications in the THz region, a critical technology to the next generation remote sensing, has not yet been explored.

Appendix A: Optical Absorption Difference Spectra
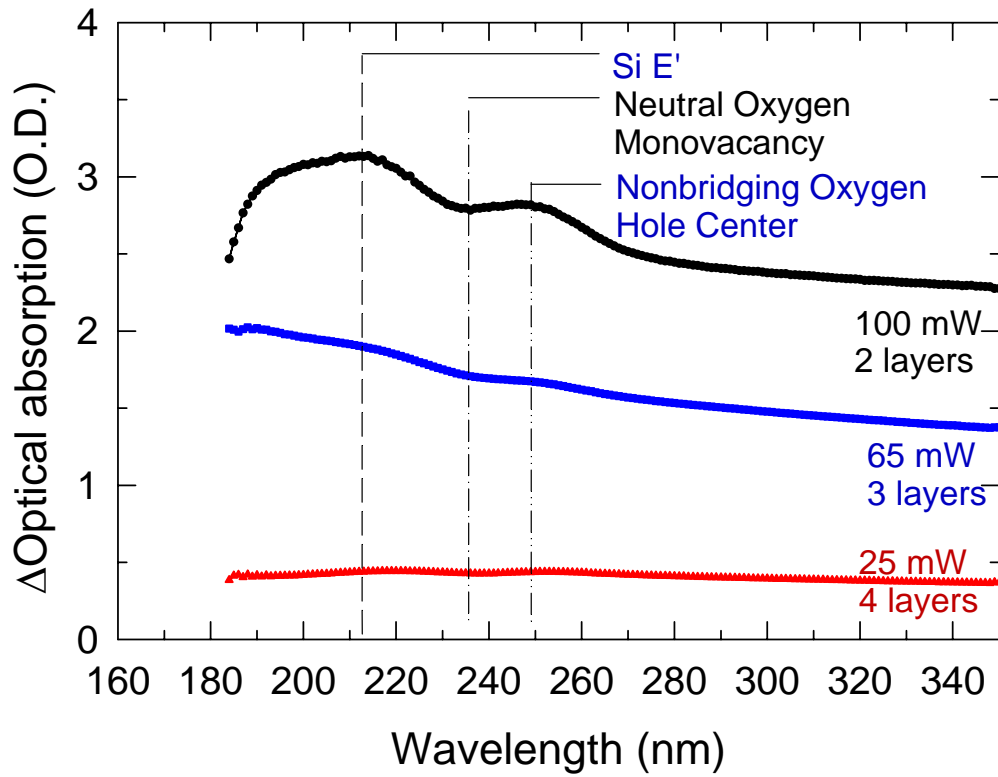
Figure BA1   Optical absorption difference spectra of femtosecond laser damaged areas.

Comments:

    Most collected signals were simply by scattering of the incident beam from a multiple layer damaged test pattern, therefore, the data are not true measurement of optical density.

Appendix B: Photoluminescence Excited by 800 nm femtosecond Laser Pulses
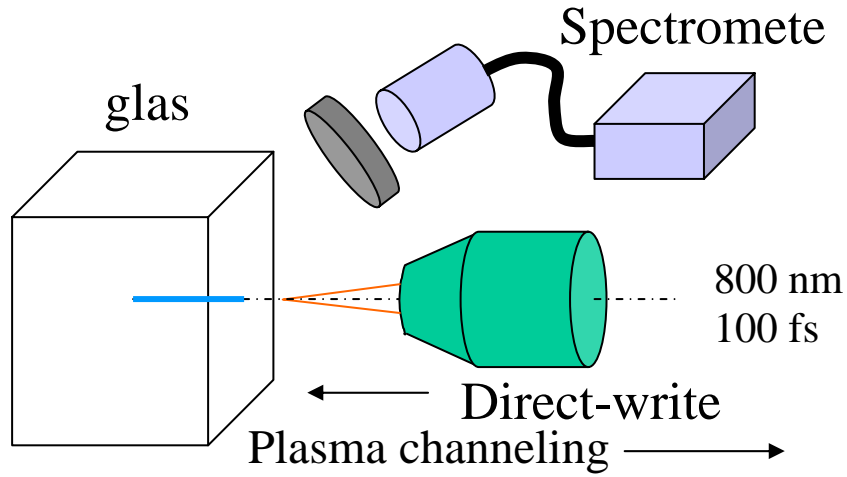
Fig. BB1. Experimental set-up for photoluminescence measurements.
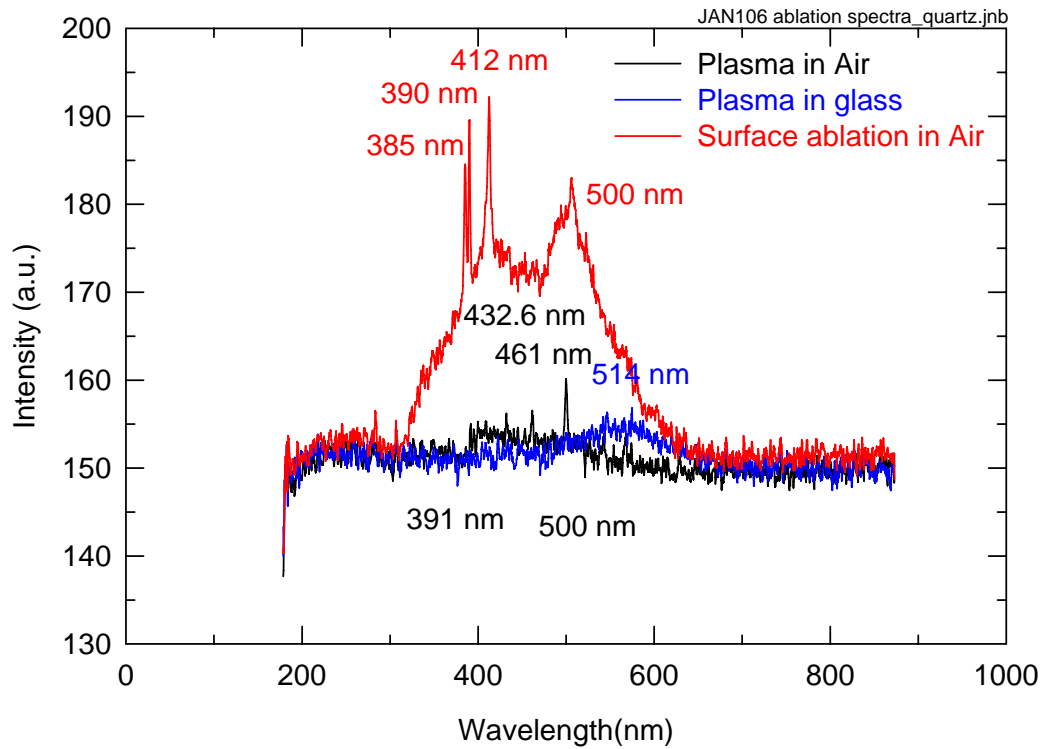
Fig BB2. Photoluminescence spectra of plasma created from air, ablation, and inside of silica.

REFERENCES

1 P. Maine, D. Strickland, P. Bada, M. Pessot, and G. Mourou, "Generation of ultrahigh peak power pulses by chirped pulse amplification," *IEEE J. Quantum Electr.* , **24**(2) 398-403 (1988).

2 K. Yamasaki, S. Juodkazis, T. Lippert, M. Watanable, S. Matsuo, and H. Hisawa, "Dielectric breakdwon of rubber materials by femtosecond irradiation," *Appl. Phys.*, **A76**(3) 325-329 (2003).

3 W. Denk, J. H. Strickler, and W. W. Webb, "Two-photon laser scanning fluorescence microscopy," *Science* **248** 73-76 (1990).

4 J. Ihlemann, B. Wolff, and P. Simon, "Nanosecond and femtosecond excimer laser ablation of fused silica," *Appl. Phys. A.*, **A64** 363-368 (1992).

5 H. Varel, D. Ashkenasi, A. Rosenfeld, M. Wahmer, and E. E. B. Campell, "Micromachining of quartz with ultrashort laser pluses," *Appl. Phys. A.*, **A65** 367-373 (1997).

6 M. D. Perry, B. C. Stuart, P. S. Banks, M. D, Feit, V. Yanovsky, and A. M. Rubenchik, "Ultrashort-pulse laser machining of dielectric materials," *J. Appl. Phys.*, **85**(9) 6803-6810 (1999).

7 E. N Glezer, M. Milosavljevic, L. Huang, R. J. Finlay, T. H. Her, J. P. Callan, and E. Mazur, "Three-dimensional optical storage inside transparent materials," *Opt. Lett.*, **21**(24), 2023-2025 (1996).

8 A. Toriumi, J. M. Herrmann, and S. Kawata, "Nondestructive readout of a three-dimensional photochromic optical memory with a near-infrared differential phase-contrast microscope," *Opt. Lett.*, **22**(8) 555-557, (1997).

9 Y. Kawata, H. Ishitobi, and S. Kawata, "Use of two-photon absorption in a photorefractive crystal for three-dimensional optical memory," *Opt. Lett.*, **23**(10) 756-758 (1998).

10 H. Misawa, S. Juodkazis, H-B. Sun, S. Matsuo, and J. Nishii, "Formation of photonic crystals by femtosecond microfabrication," *Proc. SPIE* **4088** (SPIE, Bellingham, WA) 29-32, (2000).

11 F. Garcia-Santamaria, C. Lopez, F. Messeguer, F. Lopez-Tejeira, J. Sanchez-Dehesa, and H. T. Miyazaki, "Opal-like photonic crystal with diamond lattice," *Appl. Phys. Lett.*, **79**(15) 2309-2311 (2001).

12 H-B. Sun, Y. Xu, S. Juodkazis, K. Sun, M. Watanabe, S. Matsuo, H. Misawa, and J, Nishii, "Arbitrary-lattice photonic crystals created by multiphoton microfabrication," *Opt. Lett*., **26**(6), 325-327 (2001).

13 K. Miura, J. Qiu, T. Mitsuyu, and K. Hirano, "Space-selective growth of frequency-conversion crystals in glasses with ultrashort laser pulses," *Opt. Lett*., **25**(6) 408-410, (2000).

14 K. M. Davis, K. Miura, N. Sugimoto, and K. Hirao, "Writing waveguides in glass with a femtosecond laser," *Opt. Lett*., **21**(21) 1729-1731 (1996).

15 K. Miura, J. Qiu, H. Inouye, T. Mitsuyu, and K. Hirao, "Photowritten Optical waveguides in various glasses with ultrashort pulse laser," *Appl. Phys. Lett.*, **71**(23) 3329-3331 (1997).

16 K. Simmons-Potter, B. G. Potter Jr., D. C. Meister, and M. B. Sinclair, "Photosensitive thin film materials and devices," *J. of Non-cryst. Solids*, **239** 96-103 (1998).

17 D. Homoelle, S. Wielandy, A. L. Gaeta, N. F. Borrelli, C. Smith, "Infrared photosenitivity in silica glasses exposed to femtosecond laser pulses," *Opt. Lett*., **24**(18) 1311-1313 (1999).

18 J. D. Mills, P. G. Kazansky, E. Bricchi, and J. J. Baumberg, "Embedded anisotropic microreflectors by femtosecond-laser nanomachining," *Appl. Phys. Lett*., **81**(2) 196-198 (2002).

19 E. Bricchi, J. D. Mills, P. g. Kazansky, B. G. Klappauf, and J. Baumberg, "Birefringent Fresnel zone plates in silica fabricated by femtosecond laser machining," *Opt. Lett.*, **27**(4) 2200-2202 (2002).

20 M. Masuda, K. Sugioka, Y. Chen, N. Aoki, M. Kawachi, K. Shihoyama, K. Toyoda, H. Helvajian, and K. Midorikawa, "3-D microstructure inside photosensitive glass by femtosecond laser excitation," *Appl. Phys.*, **A76** 857-860 (2003).

21 A. Marcinkevicious, S. Juodkazis, M. Watanable, M. Miwa, S. Matsuo, H. Misawa, and J. Nishii, "Femtosecond laser-assisted three-dimensional microfabrication in silica," *Opt. Lett.*, **26** (5) 277-279 (2001).

22 D. Ashkenasi, H. Varel, A. Rosenfeld, S. Henz, J. Hermann, and E. E. B. Cambell, "Application of self-focusing of ps laser pulses for three-dimensional microstructuring of transparent materials," *Appl. Phys. Lett*., **72**(12) 1442-1444 (1998).

23 A. marcinkevicius, S. Huodkazix, M. Watanable, M. Miwa, S. Matsuo, and H. Misawa, "Femtosecond laser-assisted three-dimensional microfabrication in silica." *Opt. Lett*., **26**(5) 277-279 (2001).

24 Y. Li, K. Itoh, W. Watanable, K. Yamada, D. Kuroda, J. Nishii, and Y. Jiang, "Three-dimensional hole drilling of silica glass from the rear surface with femtosecond laser pulses," *Opt. Lett*., **26**(23) 1912-1914 (2001).

25 D. J. Hwang, T. Y. Choi, and C. P. Grigoropoulos, "Liquid-assisted femtosecond laser drilling of straight and three-dimensional microchannels in glass," *Appl. Phys*., **A79** 605-612 (2004).

26 S. Cho, H. Kumagai, K. Midorikawa, and M. Obara, "Time-resolved dynamics of plasma self-channeling and bulk modification in silica glasses induced by a high-intensity femtosecond laser," *First International Symposium on Laser Precision Modification*, Editors: I. Miyamoto, K. Sugioka, and T. W. Sigmon, *Proc. SPIE* **4088**, (SPIE, Bellingham, WA) 40-43 (2000).

27 D. M. Mittleman, D. C. Douglass, Z Henis, O. R. Wood, R. R. Freeman, and T. J. Mcilrth, "High-field harmonic generation in the tight-focusing limit" *J. Opt. Soc. AM*., **B. 13(1)**, 170-179 (1996).

28 S. C. Rae and K Burnett, "Possible production of cold plasma through optical-field-induced ionization," *Phys. R ev*., **A. 46**(4), 2077-2083 (1992).

29 R. Osellame, S. Taccheo, M. Marangoni, R. Ramponi, P. Laporta, D. Polli, S. De Silvestri, and G. Gerullo, "Femtosecond Writing of Active Optical Waveguides with Astimatically Shaped Beams," *J. Opt. Soc. Am.,* **B20**(7) 1559-1567 (2003).

30 Y. Chen, K. Sugioko, K. Midorikawa, M. Masuda, K. Toyoda, M. Kawachi, and K. Shihoyama, "Control of the cross-section shape of a hollow microchannel embedded in photostructurable glass by use of a femtosecond laser," *Opt. Lett*., **28**(1) 55-57 (2003).

31 C. B. Schaffer, J. F. Garcia, and E. Mazur, "Bulk heating of transparent materials using a high-repetition-rate femtosecond laser," *Appl. Phys*., **A76** 351-354 (2003).

32 P. Yang, D. R. Tallant, G. R. Burns, and M. L. Griffith, "Femtosecond laser pulse induced refractive index changes in glass, " 2002 Material Research Society, "Femto- and Attosecond Phenomena in Material, Dec. 2-6, Boston, MA., (2002)., J. W. Chan, T. R. Huser, S. H. Risbud, and D. M. Krol, "Modification of the fused silica glass network associated with waveguide fabrication using femtosecond laser pulses" *Appl. Phys*., **A76** 367-372 (2003).

33 P. Yang, G. R. Burns, J. Guo, T. S. Luk, and A. G. Vawter, "Femtosecond laser-pulse-induced birefringence in optically isotropic glass," *J. Appl. Phys*., **95**(10) 5280-5283 (2004).

34 L. Sudrie, M. Franco, B. Prade, and A. Mysyrowicz, "Writing of permanent birefringent microlayers in bulk fused silica with femtosecond laser pulses," *Opt. Comm.*, **171** 279-284 (1999).

35 E. N. Glezer and E. Mazur, "Ultrafast-laser driven micro-explosions in transparent materials," *Appl. Phys. lett*. **71**(7), 882-884 (1997).

36 P. Yang, G. R. Burns, D. R. Tallant, J. Guo, and T. S. Luk, "Direct-write waveguides and structural modification by femtosecond laser pulses," *Proc, SPIE* **5342** (SPIE, Bellingham, WA) 146-155 (2004).

37 J. W. Chan, T. R. Huser, S. H. Risbud, and D. M. Krol, "Modification of fused silica glass network associated with waveguide fabrication using femtosecond laser pulses," *Appl. Phys*. **A76**(3) 367-372 (2003).

38 P. Yang and George R. Burns, unpublished data.

39 G. Y. Yang and Y. R. Shen, "Spectral broadening of ultrashort pulses in a nonlinear medium," *Opt. Lett*., **9**(11) 510-512 (1984).

40 A. Broder and S. L. Chin, "Band-gap dependence of the ultrafast white-light continuum," *Phys. Rev. Lett.*, **80**(20) 4406-4409 (1998).

41 F. L. Galeener, "Band limits and the vibrational spectra of tetrahedral glasses," *Phys. Rev. B*, **19** (8) 4292-4297 (1979).

42 F. Ll galeener, "Planar rings in glasses," *Solid State Comm*., **44**(7) 1037-1040 (1982).

43 F.L. Galeener, R. A. Barrio, E. Martinez, and R. J. Elliott, "Vibrational decoupling of rings in amorphous solids," *Phys. Rev. Lett*., **53**(25) 2429-2432 (1984).

44 R. J. Hemley, H. K. Mao, P. M. Bell and B. O. Mysen, "Raman spectroscopy of SiO_2 glass in high pressure," *Phys. Rev. Lett*., **57**(6) 747-750 (1986).

45 M. Okuno, B. Reynard, Y. Shimada, Y. Syono, C. Willaime, "A Raman spectroscopic study of shock wave densification of vitreous silica," *Phys. Chem. Minerals*, **26** 304-311 (1999). Y. Shimada, M. Okuno, Y. Syono, M/ Kikuchi, K. Fukuoba, N. Ishizawa, "An X-ray diffraction study of shock-wave-densified SiO_2 glasses," *Phys. Chem. Minerals*, **29** 233-239 (2002). B. Reynard, M. Okuno, Y. Shimada, Y. Syono, C. Willaime, "A Raman spectroscopic study of shock-wave densification of anorthite glass," *Phys. Chem. Minerals*, **26** 432-436 (1999).

46 C. J. Brinker, R. K. Brow, D. R. Tallant, R. J. Kirkpatrick, "Surface structure and chemistry of high surface area silica gels," *J. Non-Cryst. Solid*, **120**(1-3) 26-33, 1990, and D. R. Tallant, B. C. Bunker, C. J. Brinker, and C. A. Balfe, "Raman spectra of

rings in silicate materials," *Mater. Res. Soc. Symp.. Proc* **73** 261-271, Material Research Society, Pittsburgh, 1986.

47 D. Haaland, K. Higgins, D. R. Tallant, "Multivariate Calibration of Carbon Raman Spectra for Quantitative Determination of Peak Temperature History," *Vibrational Spectroscopy*, **1** 35-40 (1990).

48 D. R. Tallant, B. C. Bunker, C. J. Brinker, and C. A. Balfe, "Raman Spectra of Rings in Silicate Materials, " *Mater. Res. Soc. Symp. Proc*., **73** 261-271 (Material Research Society, Pittsburg) 1996.

49 N. F. Borrelli, C. M Smith, J. J. Price, and D. C. Allan, "Polarized excimer laser-induced birefringence in silica," *Appl. Phys. Lett*., **80**(2) 219-221 (2002).

50 T. Fujiwara, M. Takahashi, and A. J. Ikushima, "Second-harmonic generation in germanosilicate glass poled with ArF laser irradiation," *Appl. Phys. Lett*., **71**(8), 1032-1034 (1997).

51 W. Marguils, F. C. Garcia, E. N. Hering, L. C. Guedes Valente, B. Lesche, F. laurel, and I. C. S. Carvalho, "Poled Glass," *MRS Bull*., **33** 31-XX (1998), and references within.

52 G. Chen, H. Jain, M. Vlcek, S. Khalid, J. Li, D. A. Drabold, and S. R. Elliott, "Observation of light polarization-dependent structural changes in chalcogenide glasses," *Appl. Phys. Lett*., **82** 706-708 (2003).

53 H. K. Tönshoff, C. Momma, A. Ostendorf, S. Nolte, and G. Kamlage, "Microdrilling of metals with ultrashort laser pulse," *J. of Laser Applications*, **12**(1) 23-27 (2000).

54 N. F. Borrell, C. M. Smith, J. J. Price, and D. C. Allan, "Polarized excimer laser-induced birefringence in silica," *Appl. Phys. Lett*., **80**(2) 219-221 (2002).

55 Y. Shimotsuma, P. G. Kazansky, J. Qiu, and K. Hirao, "Self-organized nanogradings in glass irradiated by ultrashort light pulses," Phy. *Rev. Lett*., **91**(24) 247405-1 (2003).

56 M. Born and E. Wolf, *Principle of Optics*, Chapter 15, 835-840, Cambridge University Press, Cambridge, United Kingdom, 1999.

57 K. Hirao and K. Miura, "Writing waveguides and rratings in silica and related materials by a femtosecond Laser," *J. Non-Crystallline Solids*, **239**(1-3) 91-95 (1998).

58 K. Miura, J. Qiu, T. Mitsuyu, and K. Hirao, "Preparation and optical properties of fluoride glass waveguides induced by laser pulses," *J. Non-Crystalline Solid*, **256&257** 212-219 (1999).

59 M. Will, S. Nolte, B. N. Chichkov, and A. Tunnermann, "Optical properties of waveguides fabricated in fused silica by femtosecond laser pulses," *Appl. Opt.*, **41**(21) 4360-4364 (2002).

60 N. V. Nikonorov and G. T. Petrovskii, "Ion-exchange glasses in integrated optics: The current state of research and prospects," *Glass Physics and Chemistry*, **25**(1) 16-55 (1999).

61 T. Findakly, "Glass waveguides by ion exchange: a review," *Opt. Eng.*, **24**(2), 244-250 (1985).

62 M. Hirano, K-I Kawamura, and H. Hosono, "Encoding of holographic grating and periodic nano-structure by femtosecon laser pulse," *Appl. Surface Sci.*, **197-198,** 688-698 (2002).

63 A. M. Streltsov and N. F. Borrelli, "Fabrication and analysis of a directional coupler written in glass by nanojoule femtosecond laser pulses," *Opt. Lett.*, **26**(1) 42-43 (2001).

64 R. Gao, J. Zhang, L. Zhang, J. Sun, X. Kong, H. Song, J. Zheng, "Femtosecond laser induced optical waveguides and micro-mirrors inside glasses," *Chin. Phys. Lett.*, **19**(10) 1424-1426 (2002).

Distribution:

1   MS0188   LDRD Office
4   MS0959   P. Yang
1   MS0959   G. R. Burns
1   MS0959   T. Gardner
1   MS0961   C. Adkins
2   MS0958   J. A. Palmer
1   MS0958   M. F. Harris
1   MS0958   G. L. Benavades
1   MS0961   J. Harris
1   MS0374   K. L. McDaniel
1   MS0603   G. A. Vawter
1   MS0603   C. T. Sullivan
1   MS1411   D.R. Tallant
1   MS0311   M. L. Griffith
1   MS1153   T. S. Luk
1   MS9018   Center Technical Files, 8945-1
2   MS0899   Technical Library, 9616